

Wasserstein Iterative Networks for Barycenter Estimation

Alexander Korotin^{1,2} Vage Egiazarian¹ Lingxiao Li³ Evgeny Burnaev^{1,2}

Abstract

Wasserstein barycenters have become popular due to their ability to represent the average of probability measures in a geometrically meaningful way. In this paper, we present an *algorithm* to approximate the Wasserstein-2 barycenters of continuous measures via a generative model. Previous approaches rely on regularization (entropic/quadratic) which introduces bias or on input convex neural networks which are not expressive enough for large-scale tasks. In contrast, our algorithm does not introduce bias and allows using arbitrary neural networks. In addition, based on the celebrity faces dataset, we construct Ave, celeba! dataset which can be used for quantitative evaluation of barycenter algorithms by using standard metrics of generative models such as FID.

1. Introduction

Wasserstein barycenters (Agueh & Carlier, 2011) provide a geometrically meaningful notion of the average of probability measures based on optimal transport (OT, see (Vilani, 2008)). Methods for computing barycenters have been successfully applied to various practical problems. In geometry processing, shape interpolation can be performed by barycenters (Solomon et al., 2015). In image processing, barycenters are used for color and style translation (Rabin et al., 2014; Mroueh, 2019), texture mixing (Rabin et al., 2011) and image interpolation (Lacombe et al., 2021; Simon & Aberdam, 2020). In language processing, barycenters can be applied to text evaluation (Colombo et al., 2021). In online learning, barycenters are used for aggregating probabilistic forecasts of experts (Korotin et al., 2021d; Paris, 2021). In Bayesian inference, the barycenter of subset posteriors converges to the full data posterior (Srivastava et al., 2015; 2018) allowing efficient computations of full posterior based on barycenters. In reinforcement learning, barycenters are used for uncertainty propagation (Metelli et al.,

¹Skolkovo Institute of Science and Technology, Moscow, Russia ²AIRI, Moscow, Russia ³Massachusetts Institute of Technology, Cambridge, Massachusetts, USA. Correspondence to: Alexander Korotin <a.korotin@skoltech.ru>.

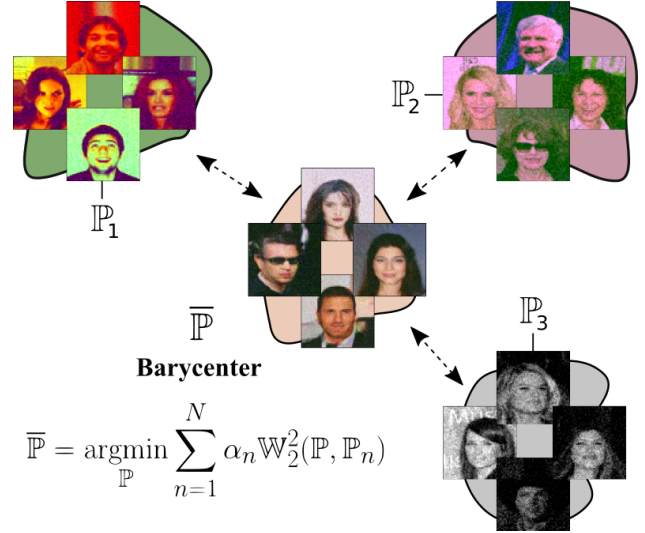


Figure 1: The barycenter w.r.t. $(\alpha_1, \alpha_2, \alpha_3) = (\frac{1}{4}, \frac{1}{2}, \frac{1}{4})$ of Ave, Celeba! subsets computed by our Algorithm 1.

The figure shows random samples from the input subsets and generated images from the barycenter.

2019). Other applications include data augmentation (Bespalov et al., 2021), multivariate density registration (Bigot et al., 2019), distributions alignment (Inouye et al., 2021), domain generalization (Lyu et al., 2021) and adaptation (Montesuma & Mboula, 2021), model ensembling (Dognin et al., 2019).

The bottleneck of obtaining barycenters is the computational complexity. For *discrete* measures, fast and accurate barycenter algorithms exist for low-dimensional problems; see (Peyré et al., 2019) for a survey. However, discrete methods scale poorly with the number of support points of the barycenter. Consequently, they cannot approximate continuous barycenters well, especially in high dimensions.

For *continuous* measures, only a few algorithms exist (Li et al., 2020; Fan et al., 2020; Korotin et al., 2021c). Existing continuous barycenter approaches are based on entropic/quadratic regularization, or parametrization of Brenier potentials with input-convex neural networks (ICNNs, see (Amos et al., 2017)). The regularization-based [CRWB] algorithm by (Li et al., 2020) recovers a barycenter *biased* from the true one. Algorithms [CW₂B] by (Korotin et al., 2021c) and [SCW₂B] by (Fan et al., 2020) based on ICNNs resolve this issue, see (Korotin et al., 2021c, Tables 1-3).

However, despite the growing popularity of ICNNs in OT applications (Makkuva et al., 2019; Korotin et al., 2021a; Mokrov et al., 2021), they could be suboptimal architectures according to a recent study (Korotin et al., 2021b). According to the authors, more expressive networks without the convexity constraint outperform ICNNs in practical OT problems.

On the other hand, *evaluation* of barycenter algorithms is challenging due to limited number of continuous measures with explicitly known barycenter. It can be computed in the Gaussian and location-scatter cases (Álvarez-Esteban et al., 2016, §4) and the 1-dimensional case (Bonneel et al., 2015, §2.3). Recent works (Li et al., 2020; Korotin et al., 2021c; Fan et al., 2020) consider the Gaussian case in dimensions ≤ 256 for quantitative evaluation. In higher dimensions, the computation of the ground truth barycenter is hard even for the Gaussian case: it involves matrix inversion and square root extraction (Altschuler et al., 2021, Algorithm 1) with the cubic complexity in the dimension of the ambient space.

Contributions.

- We develop a novel *iterative algorithm* (§4) for estimating Wasserstein-2 barycenters based on the fixed point approach by (Álvarez-Esteban et al., 2016) combined with a neural solver for optimal transport (Korotin et al., 2021b). Unlike predecessors, our algorithm does not introduce bias and allows arbitrary network architectures.
- We construct the *Ave, celebra!* (averaging celebrity faces, §5) dataset consisting of 64×64 RGB images for large-scale quantitative evaluation of continuous Wasserstein-2 barycenter algorithms. The dataset includes 3 subsets of degraded images of faces. The barycenter of these subsets corresponds to the original clean faces.

Our algorithm is suitable for large-scale Wasserstein-2 barycenters applications. The developed dataset will allow quantitative evaluation of barycenter algorithms at a large scale improving transparency and providing healthy competition in the optimal transport research.

Notation. We work in a Euclidean space \mathbb{R}^D for some D . All the integrals are computed over \mathbb{R}^D if not stated otherwise. We denote the set of all Borel probability measures on \mathbb{R}^D with finite second moment by $\mathcal{P}_2(\mathbb{R}^D)$. We use $\mathcal{P}_{2,ac}(\mathbb{R}^D) \subset \mathcal{P}_2(\mathbb{R}^D)$ to denote the subset of absolutely continuous measures. We denote its subset of measures with positive density by $\mathcal{P}_{2,ac}^+(\mathbb{R}^D) \subset \mathcal{P}_{2,ac}(\mathbb{R}^D)$. We denote the set of probability measures on $\mathbb{R}^D \times \mathbb{R}^D$ with marginals \mathbb{P} and \mathbb{Q} by $\Pi(\mathbb{P}, \mathbb{Q})$. For a measurable map $T : \mathbb{R}^D \rightarrow \mathbb{R}^D$, we denote the associated push-forward operator by $T\#$. For $\phi : \mathbb{R}^D \rightarrow \mathbb{R}$, we denote by $\bar{\phi}$ its Legendre-Fenchel transform (Fenchel, 1949) defined by $\bar{\phi}(y) = \max_{x \in \mathbb{R}^D} [\langle x, y \rangle - \phi(x)]$. Recall that $\bar{\phi}$ is a convex function, even when ϕ is not.

2. Preliminaries

Wasserstein-2 distance. For $\mathbb{P}, \mathbb{Q} \in \mathcal{P}_2(\mathbb{R}^D)$, Monge’s *primal* formulation of the squared Wasserstein-2 distance, i.e., OT with *quadratic cost*, is

$$\mathbb{W}_2^2(\mathbb{P}, \mathbb{Q}) \stackrel{\text{def}}{=} \min_{T\#\mathbb{P}=\mathbb{Q}} \int \frac{1}{2} \|x - T(x)\|^2 d\mathbb{P}(x), \quad (1)$$

where the minimum is taken over measurable functions (transport maps) $T : \mathbb{R}^D \rightarrow \mathbb{R}^D$ mapping \mathbb{P} to \mathbb{Q} . The optimal T^* is called the *optimal transport map*. Note that (1) is not symmetric, and this formulation does not allow for mass splitting, i.e., for some $\mathbb{P}, \mathbb{Q} \in \mathcal{P}_2(\mathbb{R}^D)$, there might be no map T that satisfies $T\#\mathbb{P} = \mathbb{Q}$. Thus, (Kantorovitch, 1958) proposed the following relaxation:

$$\mathbb{W}_2^2(\mathbb{P}, \mathbb{Q}) \stackrel{\text{def}}{=} \min_{\pi \in \Pi(\mathbb{P}, \mathbb{Q})} \int_{\mathbb{R}^D \times \mathbb{R}^D} \frac{1}{2} \|x - y\|^2 d\pi(x, y), \quad (2)$$

where the minimum is taken over all transport plans π , i.e., measures on $\mathbb{R}^D \times \mathbb{R}^D$ whose marginals are \mathbb{P} and \mathbb{Q} . The optimal $\pi^* \in \Pi(\mathbb{P}, \mathbb{Q})$ is called the *optimal transport plan*. If π^* is of the form $[\text{id}, T^*]\#\mathbb{P} \in \Pi(\mathbb{P}, \mathbb{Q})$ for some T^* , then T^* minimizes (1).

The *dual form* (Villani, 2003) of \mathbb{W}_2^2 is:

$$\mathbb{W}_2^2(\mathbb{P}, \mathbb{Q}) = \max_{u \oplus v \leq \frac{\|\cdot\|^2}{2}} \left[\int u(x) d\mathbb{P}(x) + \int v(y) d\mathbb{Q}(y) \right], \quad (3)$$

where the maximum is taken over $u \in \mathcal{L}^1(\mathbb{P})$, $v \in \mathcal{L}^1(\mathbb{Q})$ satisfying $u(x) + v(y) \leq \frac{1}{2} \|x - y\|^2$ for all $x, y \in \mathbb{R}^D$. The functions u and v are called *potentials*.

There exist optimal u^*, v^* satisfying $u^* = (v^*)^c$, where $f^c : \mathbb{R}^D \rightarrow \mathbb{R}$ is the c -transform of f defined by $f^c(y) = \min_{x \in \mathbb{R}^D} [\frac{1}{2} \|x - y\|^2 - f(x)]$. We can rewrite (3) as

$$\mathbb{W}_2^2(\mathbb{P}, \mathbb{Q}) = \max_v \left[\int v^c(x) d\mathbb{P}(x) + \int v(y) d\mathbb{Q}(y) \right], \quad (4)$$

where the maximum is taken over all $v \in \mathcal{L}^1(\mathbb{Q})$.

It is customary (Villani, 2008, Cases 5.3 & 5.17) to define $u(x) = \frac{1}{2} \|x\|^2 - \psi(x)$ and $v(y) = \frac{1}{2} \|y\|^2 - \phi(y)$. There exist convex optimal ψ^* and ϕ^* satisfying $\bar{\psi}^* = \phi^*$ and $\bar{\phi}^* = \psi^*$.

If $\mathbb{P} \in \mathcal{P}_{2,ac}(\mathbb{R}^D)$, then the optimal T^* of (1) always exists and can be recovered from the dual solution u^* (or ψ^*) of (3): $T^*(x) = x - \nabla u^*(x) = \nabla \psi^*(x)$ (Santambrogio, 2015, Theorem 1.17). Map T^* is a gradient of a convex function, the fact known as the Brenier Theorem (Brenier, 1991).

Wasserstein-2 barycenter. Let $\mathbb{P}_1, \dots, \mathbb{P}_N \in \mathcal{P}_{2,ac}(\mathbb{R}^D)$ such that at least one of them has bounded density. Their barycenter w.r.t. weights $\alpha_1, \dots, \alpha_N$ ($\alpha_n > 0$; $\sum_{n=1}^N \alpha_n = 1$) is given by (Agueh & Carlier, 2011):

$$\bar{\mathbb{P}} \stackrel{\text{def}}{=} \arg \min_{\mathbb{P} \in \mathcal{P}_2(\mathbb{R}^D)} \sum_{n=1}^N \alpha_n \mathbb{W}_2^2(\mathbb{P}_n, \mathbb{P}). \quad (5)$$

The barycenter $\bar{\mathbb{P}}$ exists uniquely such that $\bar{\mathbb{P}} \in \mathcal{P}_{2,ac}(\mathbb{R}^D)$. Moreover, its density is bounded (Agueh & Carlier, 2011, Definition 3.6 & Theorem 5.1).

For $n \in \{1, 2, \dots, N\}$, let $T_{\bar{\mathbb{P}} \rightarrow \mathbb{P}_n} = \nabla \psi_n^*$ be the OT maps from $\bar{\mathbb{P}}$ to \mathbb{P}_n . The following holds $\bar{\mathbb{P}}$ -almost everywhere:

$$\sum_{n=1}^N \alpha_n T_{\bar{\mathbb{P}} \rightarrow \mathbb{P}_n}(x) = \sum_{n=1}^N \alpha_n \nabla \psi_n^*(x) = x, \quad (6)$$

see (Álvarez-Esteban et al., 2016, §3). If $\bar{\mathbb{P}} \in \mathcal{P}_{2,ac}^+(\mathbb{R}^D)$, then (6) holds for every $x \in \mathbb{R}^D$, i.e., $\sum_{n=1}^N \alpha_n \psi_n^*(x) = \frac{\|x\|^2}{2} + c$. We call such convex potentials ψ_n^* *congruent*.

3. Related Work

Below we review existing continuous methods for OT. In §3.1, we discuss methods for OT problems (1), (2), (3). In §3.2, we review algorithms that compute barycenters (5).

3.1. Continuous OT Solvers for \mathbb{W}_2

We use the phrase *OT solver* to denote any method capable of recovering the OT map T^* or the potential u^* (or ψ^*).

Primal-form solvers based on (1) or (2), e.g., (Xie et al., 2019; Lu et al., 2020), parameterize T^* using complicated generative modeling techniques with adversarial losses to handle the pushforward constraint $T\#\mathbb{P} = \mathbb{Q}$ in the primal form (1). They depend on careful hyperparameter search and complex optimization (Lucic et al., 2018).

Dual-form continuous solvers (Genevay et al., 2016; Seguy et al., 2017; Nhan Dam et al., 2019; Taghvaei & Jalali, 2019; Korotin et al., 2021a) based on (3) or (4) have straightforward optimization procedures and can be adapted to various tasks without extensive hyperparameter search.

A comprehensive overview and a benchmark of dual-form solvers are given in (Korotin et al., 2021b). According to the evaluation, the best performing OT solver is *reversed maximin solver* [MM:R], a modification of the idea proposed by (Nhan Dam et al., 2019) in the context of Wasserstein-1 GANs (Arjovsky et al., 2017). In this paper, we employ this solver as a part of our algorithm. We review it below.

Reversed Maximin Solver. In (4), $v^c(x)$ can be expanded through v via the definition of c -transform:

$$\begin{aligned} \max_v \int \min_{y \in \mathbb{R}^D} \left[\frac{\|x - y\|_2^2}{2} - v(y) \right] d\mathbb{P}(x) + \int v(y) d\mathbb{Q}(y) = \\ \max_v \min_T \int \left[\frac{\|x - T(x)\|_2^2}{2} - v(T(x)) \right] d\mathbb{P}(x) + \int v(y) d\mathbb{Q}(y). \end{aligned} \quad (7)$$

In the derivations above, the optimization over $y \in \mathbb{R}^D$ is replaced by the equivalent optimization over functions $T : \mathbb{R}^D \rightarrow \mathbb{R}^D$. This is done by the interchanging of integral and minimum, see (Rockafellar, 1976, Theorem 3A).

The key point of this reformulation is that the optimal solution of this maximin problem is given by (v^*, T^*) , where T^* is the OT map from \mathbb{P} to \mathbb{Q} . See discussion in (Korotin et al., 2021b, §2) or (Rout et al., 2021, §4.1).

In practice, the potential $v : \mathbb{R}^D \rightarrow \mathbb{R}$ and the map $T : \mathbb{R}^D \rightarrow \mathbb{R}^D$ are parametrized by neural networks v_ω, T_θ . To train θ and ω , stochastic gradient ascent/descent (SGAD) over mini-batches from \mathbb{P}, \mathbb{Q} is used.

3.2. Algorithms for Continuous \mathbb{W}_2 Barycenters

Variational optimization. Problem (5) is optimization over probability measures. To estimate $\bar{\mathbb{P}}$, one may employ a generator network $G_\xi : \mathbb{R}^H \rightarrow \mathbb{R}^D$ with a latent measure \mathbb{S} on \mathbb{R}^H and train ξ by minimizing

$$\sum_{n=1}^N \alpha_n \mathbb{W}_2^2(\overbrace{G_\xi \#\mathbb{S}}^{\mathbb{P}_\xi}, \mathbb{P}_n) \rightarrow \min_\xi. \quad (8)$$

Optimization (8) can be performed by using SGD on random mini-batches from the measure \mathbb{S} and measures \mathbb{P}_n .

The difference between possible variational algorithms lies in the particular estimation method for \mathbb{W}_2^2 terms. To our knowledge, only ICNN-based minimax solver (Makkuva et al., 2019) has been used to compute \mathbb{W}_2^2 in (8) yielding [SC \mathbb{W}_2 B] algorithm (Fan et al., 2020).

Potential-based optimization. (Li et al., 2020; Korotin et al., 2021c) recover the optimal potentials $\{\psi_n^*, \phi_n^*\}$ for each pair $(\bar{\mathbb{P}}, \mathbb{P}_n)$ via a non-minimax regularized dual formulation. No generative model is needed: the barycenter is recovered by pushing forward measures using gradients of potentials or by barycentric projection. However, the non-trivial choice of the *prior* barycenter distribution is required. Algorithm [CRWB] by (Li et al., 2020) uses entropic or quadratic regularization and [CW $_2$ B] algorithm by (Korotin et al., 2021c) uses ICNNs, congruence and cycle-consistency (Korotin et al., 2021a) regularization.

4. Iterative \mathbb{W}_2 -Barycenter Algorithm

Our proposed algorithm is based on the *fixed point approach* by (Álvarez-Esteban et al., 2016) which we recall in §4.1. In §4.2, we formulate our algorithm for computing Wasserstein-2 barycenters. In §4.3, we show that our algorithm generalizes the variational barycenter approach.

4.1. Theoretical Fixed Point Approach

Following (Álvarez-Esteban et al., 2016), we define an operator $\mathcal{H} : \mathcal{P}_{2,ac}(\mathbb{R}^D) \rightarrow \mathcal{P}_{2,ac}(\mathbb{R}^D)$ by

$$\mathcal{H}(\mathbb{P}) = \left[\sum_{n=1}^N \alpha_n T_{\mathbb{P} \rightarrow \mathbb{P}_n} \right] \#\mathbb{P}, \quad (9)$$

where $T_{\mathbb{P} \rightarrow \mathbb{P}_n}$ denotes the OT map from \mathbb{P} to \mathbb{P}_n . The measure $\mathcal{H}(\mathbb{P})$ obtained by the operator is indeed absolutely continuous, see (Álvarez-Esteban et al., 2016, Theorem 3.1). According to (6), the barycenter $\bar{\mathbb{P}}$ defined by (5) is a *fixed point* of operator \mathcal{H} , i.e., $\mathcal{H}(\bar{\mathbb{P}}) = \bar{\mathbb{P}}$. This suggests a way to compute $\bar{\mathbb{P}}$ by picking some $\mathbb{P} \in \mathcal{P}_{2,ac}(\mathbb{R}^D)$ and recursively applying operator \mathcal{H} until convergence. However, there are several **challenges**:

(a) A fixed point $\mathbb{P} \in \mathcal{P}_{2,ac}(\mathbb{R}^D)$ satisfying $\mathcal{H}(\mathbb{P}) = \mathbb{P}$ may be not the barycenter (Álvarez-Esteban et al., 2016, Example 3.1). The situation is analogous to that with the iterative k -means algorithm for a different problem – clustering. There may be fixed points which are not optimal.

(b) The sequence $\{\mathcal{H}^k(\mathbb{P})\}_k$ is tight (Álvarez-Esteban et al., 2016, Theorem 3.6) so it has a subsequence converging in $\mathcal{P}_{2,ac}(\mathbb{R}^D)$, but the entire sequence may not converge. Nevertheless, the value of the objective (5) decreases for $\mathcal{H}^k(\mathbb{P})$ as $k \rightarrow \infty$ (Álvarez-Esteban et al., 2016, Prop. 3.3).

(c) Efficient parametrization of the evolving measure $\mathcal{H}^k(\mathbb{P})$ is required. In addition, to get $\mathcal{H}^{k+1}(\mathbb{P})$ from $\mathcal{H}^k(\mathbb{P})$, one needs to compute N optimal transport maps $T_{\mathcal{H}^k(\mathbb{P}) \rightarrow \mathbb{P}_n}$ which can be costly.

Chewi et al. (2020) and Altschuler et al. (2021) consider the fixed point approach in the Gaussian case where the sequence $\mathcal{H}^k(\mathbb{P})$ is guaranteed to converge to the unique fixed point – the barycenter. The Gaussian case also makes parameterization (c) simple since both measures \mathbb{P}_n and $\mathcal{H}^k(\mathbb{P})$ can be parametrized by means and covariance matrices, and the maps $T_{\mathcal{H}^k(\mathbb{P}) \rightarrow \mathbb{P}_n}$ are linear with closed form.

For general continuous measures \mathbb{P}_n , it remains an open problem to find sharp conditions on inputs \mathbb{P}_n and the initial measure \mathbb{P} of the fixed-point iteration for the sequence $\{\mathcal{H}^k(\mathbb{P})\}_k$ to converge to the barycenter. In this work, we empirically verify that the fixed point approach works well for the input measures that we consider and for a randomly initialized generative model representing the evolving barycenter (§4.2). We tackle challenge (c) and develop a scalable optimization procedure that requires only sample access to $\mathbb{P}_n \in \mathcal{P}_{2,ac}(\mathbb{R}^D)$.

4.2. Practical Iterative Optimization Procedure

We employ a generative model to parametrize the evolving measure, i.e., put $\mathbb{P}_\xi = G_\xi \# \mathbb{S}$, where \mathbb{S} is a latent measure, e.g., $\mathbb{S} = \mathcal{N}(0, I_H)$, and G_ξ is a neural network $\mathbb{R}^H \rightarrow \mathbb{R}^D$ with parameters ξ . Our approach to compute the operator $\mathcal{H}(\mathbb{P}_\xi)$ and update G_ξ consists of two steps.

First, we approximately recover N maps $T_{\mathbb{P}_\xi \rightarrow \mathbb{P}_n}$ via [MM:R] solver, i.e., we use N pairs or networks $\{T_{\theta_n}, v_{\omega_n}\}$ and train them by optimizing (7) with $\mathbb{P} \leftarrow \mathbb{P}_\xi$

Algorithm 1: Wasserstein Iterative Networks

Input : latent \mathbb{S} and input $\mathbb{P}_1, \dots, \mathbb{P}_N$ measures;
 weights $\alpha_1, \dots, \alpha_N > 0$ ($\sum_{n=1}^N \alpha_n = 1$);
 number of iters per network: K_G, K_T, K_v ;
 generator $G_\xi : \mathbb{R}^H \rightarrow \mathbb{R}^D$;
 mapping networks $T_{\theta_1}, \dots, T_{\theta_N} : \mathbb{R}^D \rightarrow \mathbb{R}^D$;
 potentials $v_{\omega_1}, \dots, v_{\omega_N} : \mathbb{R}^D \rightarrow \mathbb{R}$;
 regression loss $\ell : \mathbb{R}^D \times \mathbb{R}^D \rightarrow \mathbb{R}_+$;

Output : generator satisfying $G_\xi \# \mathbb{S} \approx \bar{\mathbb{P}}$;
 OT maps satisfying $T_{\theta_n} \# (G_\xi \# \mathbb{S}) \approx \mathbb{P}_n$;

repeat
 # OT solvers update
for $n = 1, 2, \dots, N$ **do**
 for $k_v = 1, 2, \dots, K_v$ **do**
 Sample batches $Z \sim \mathbb{S}, Y \sim \mathbb{P}_n; X \leftarrow G_\xi(Z)$;
 $\mathcal{L}_v \leftarrow \frac{1}{|X|} \sum_{x \in X} v_{\omega_n}(T_{\theta_n}(x)) - \frac{1}{|Y|} \sum_{y \in Y} v_{\omega_n}(y)$;
 Update ω_n by using $\frac{\partial \mathcal{L}_v}{\partial \omega_n}$;
 for $k_T = 1, 2, \dots, K_T$ **do**
 Sample batch $Z \sim \mathbb{S}; X \leftarrow G_\xi(Z)$;
 $\mathcal{L}_T \leftarrow \frac{1}{|X|} \sum_{x \in X} [\frac{1}{2} \|x - T_{\theta_n}(x)\|^2 - v_{\omega_n}(T_{\theta_n}(x))]$;
 Update θ_n by using $\frac{\partial \mathcal{L}_T}{\partial \theta_n}$;
 # Generator update (regression)
 $G_{\xi_0} \leftarrow \text{copy}(G_\xi)$;
 for $k_G = 1, 2, \dots, K_G$ **do**
 Sample batch $Z \sim \mathbb{S}$;
 $\mathcal{L}_G \leftarrow \frac{1}{|Z|} \sum_{z \in Z} \ell(G_\xi(z), \sum_{n=1}^N \alpha_n T_{\theta_n}(G_{\xi_0}(z)))$;
 Update ξ by using $\frac{\partial \mathcal{L}_G}{\partial \xi}$;

until not converged

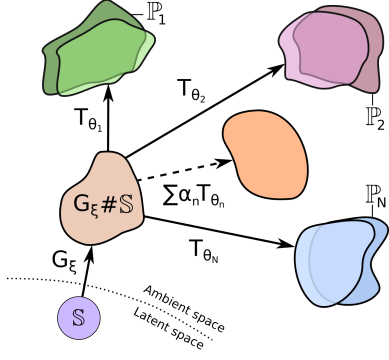
and $\mathbb{Q} \leftarrow \mathbb{P}_n$. For each $n = 1, 2, \dots, N$, we perform SGAD by using batches from $G_\xi \# \mathbb{S}$ and \mathbb{P}_n and get $T_{\theta_n} \approx T_{\mathbb{P}_\xi \rightarrow \mathbb{P}_n}$.

Second, we update G_ξ to represent $\mathcal{H}(\mathbb{P}_\xi)$ instead of \mathbb{P}_ξ . We do this via regression, the approach inspired by (Chen et al., 2019). We introduce G_{ξ_0} , a fixed copy of G_ξ . Next, we regress generator $G_\xi(\cdot)$ onto $\sum_{n=1}^N \alpha_n T_{\theta_n}(G_{\xi_0}(\cdot))$

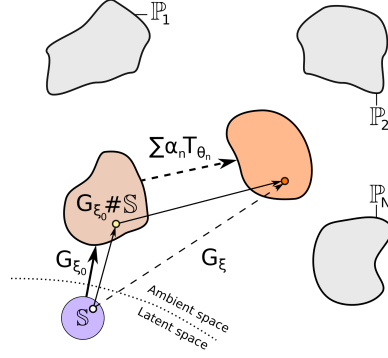
$$\int_z \ell\left(G_\xi(z), \sum_{n=1}^N \alpha_n T_{\theta_n}(G_{\xi_0}(z))\right) d\mathbb{S}(z) \rightarrow \min_{\xi}$$

by performing SGD on random batches from \mathbb{S} , e.g., by using *squared error* $\ell(x, x') \stackrel{\text{def}}{=} \frac{1}{2} \|x - x'\|^2$. As a result, generator $G_\xi(\cdot)$ becomes close to $\sum_{n=1}^N \alpha_n T_{\theta_n}(G_{\xi_0}(\cdot))$ as a function $\mathbb{R}^H \rightarrow \mathbb{R}^D$. Consequently, we get

$$\mathbb{P}_\xi = G_\xi \# \mathbb{S} \approx \left[\sum_{n=1}^N \alpha_n T_{\theta_n} \right] \# [G_{\xi_0} \# \mathbb{S}] =$$



(a) **Step 1.** We compute N approximate OT maps T_{θ_n} from generated measure $\mathbb{P}_\xi = G_\xi \# \mathbb{S}$ to input measures \mathbb{P}_n .



(b) **Step 2.** We regress $G_\xi(\cdot)$ onto $\sum_{n=1}^N \alpha_n T_{\theta_n}(G_{\xi_0}(\cdot))$, where G_{ξ_0} is a fixed copy of G_ξ before the update.

Figure 2: Our proposed two-step implementation of the fixed-point operator $\mathcal{H}(\cdot)$ that we use to compute the barycenter.

$$\left[\sum_{n=1}^N \alpha_n T_{\theta_n} \right] \# \mathbb{P}_{\xi_0} \approx \left[\sum_{n=1}^N \alpha_n T_{\mathbb{P}_{\xi_0} \rightarrow \mathbb{P}_n} \right] \# \mathbb{P}_{\xi_0} = \mathcal{H}(\mathbb{P}_{\xi_0}),$$

i.e. new generated $G_\xi \# \mathbb{S}$ measure approximates $\mathcal{H}(\mathbb{P}_{\xi_0})$.

Summary. Our two-step approach iteratively recomputes OT maps $T_{\mathbb{P}_\xi \rightarrow \mathbb{P}_n}$ (Figure 2a) and then uses regression to update the generator (Figure 2b). The *optimization procedure* is detailed in Algorithm 1. Note that when fitting OT maps $T_{\mathbb{P}_\xi \rightarrow \mathbb{P}_n}$, we start from previously used $\{T_{\theta_n}, v_{\omega_n}\}$ rather than re-initialize them. Empirically, this works better.

4.3. Relation to Variational Barycenter Algorithms

We show that our Algorithm 1 reduces to variational approach (§3.2) when the number of generator updates, K_G , is equal to 1. More specifically, we show the equivalence of the gradient update w.r.t. parameters ξ of the *generator* in our iterative Algorithm 1 and that of (8). We assume that \mathbb{W}_2^2 terms are computed exactly in (8) regardless of the particular OT solver. Similarly, in Algorithm 1, we assume that maps $G_{\xi_0} \# \mathbb{S} \rightarrow \mathbb{P}_n$ before the generator update are always exact, i.e., $T_{\theta_n} = T_{\mathbb{P}_{\xi_0} \rightarrow \mathbb{P}_n}$.

Lemma 1. Assume that $\mathbb{P}_\xi = G_\xi \# \mathbb{S} \in \mathcal{P}_{2,ac}(\mathbb{R}^D)$. Consider $K_G = 1$ for the iterative Algorithm 1, i.e., we do a single gradient step regression update per OT solvers' update. Assume that $\ell(x, x') = \frac{1}{2} \|x - x'\|^2$, i.e., the squared loss is used for regression. Then the generator's gradient update in Algorithm 1 is the same as in the variational algorithm:

$$\frac{\partial}{\partial \xi} \int_z \frac{1}{2} \|G_\xi(z) - \sum_{n=1}^N \alpha_n T_{\mathbb{P}_{\xi_0} \rightarrow \mathbb{P}_n}(G_{\xi_0}(z))\|^2 d\mathbb{S}(z) = \frac{\partial}{\partial \xi} \sum_{n=1}^N \alpha_n \mathbb{W}_2^2(G_\xi \# \mathbb{S}, \mathbb{P}_n), \quad (10)$$

where the derivatives are evaluated at $\xi = \xi_0$.

We prove the lemma in Appendix A. In practice, we choose $K_G = 50$ as we found it empirically works better.

5. Ave, celeba! Images Dataset

In this section, we develop a generic methodology for building probability measures with known \mathbb{W}_2 barycenter. We then use the methodology to construct Ave, celeba! dataset for quantitative evaluation of barycenter algorithms.

Key idea. Consider $\alpha_1, \dots, \alpha_N > 0$ with $\sum_{n=1}^N \alpha_n = 1$, congruent convex functions $\psi_1, \dots, \psi_N : \mathbb{R}^D \rightarrow \mathbb{R}$ and a measure $\mathbb{P} \in \mathcal{P}_{2,ac}^+(\mathbb{R}^D)$ with positive density. Define $\mathbb{P}_n = \nabla \psi_n \# \mathbb{P}$. Thanks to the Brenier's theorem (Brenier, 1991), $\nabla \psi_n$ is the unique OT map from \mathbb{P} to \mathbb{P}_n . Since the support of \mathbb{P} is \mathbb{R}^D , ψ_n is the unique (up to a constant) dual potential for $(\mathbb{P}, \mathbb{P}_n)$, see (Staudt et al., 2022). Since potentials ψ_n are congruent, the barycenter $\bar{\mathbb{P}}$ of \mathbb{P}_n w.r.t. weights $\alpha_1, \dots, \alpha_N$ is \mathbb{P} itself (Chewi et al., 2020, C.2). If ψ_n are such that all \mathbb{P}_n are absolutely continuous, then $\bar{\mathbb{P}} = \mathbb{P}$ is the unique barycenter (§2).

If one obtains N congruent ψ_n , then for any $\mathbb{P} \in \mathcal{P}_{2,ac}(\mathbb{R}^D)$, pushforward measures $\mathbb{P}_n = \nabla \psi_n \# \mathbb{P}$ can be used as the input measures for the barycenter task. For \mathbb{P} accessible by samples, measures \mathbb{P}_n are also accessible by samples: one may sample $x \sim \mathbb{P}$ and push samples forward by $\nabla \psi_n$.

The challenging part is to construct non-trivial congruent convex functions ψ_n . First, we provide a novel method to transform a single convex function ψ into a pair (ψ^l, ψ^r) of convex functions satisfying $\alpha \nabla \psi^l(x) + (1-\alpha) \nabla \psi^r(x) = x$ for all $x \in \mathbb{R}^D$ (Lemma 2). Next, we extend the method to generate congruent N -tuples (Lemma 3).

Lemma 2 (Constructing congruent pairs). Let ψ be a strongly convex and L -smooth (for some $L > 0$) function. Let $\beta \in (0, 1)$. Define β -left and β -right functions of ψ by

$$\psi^l \stackrel{\text{def}}{=} \beta \frac{\|\cdot\|^2}{2} + (1-\beta)\psi; \quad \psi^r \stackrel{\text{def}}{=} (1-\beta) \frac{\|\cdot\|^2}{2} + \beta\bar{\psi}. \quad (11)$$

Then $\beta \psi^l(x) + (1-\beta) \psi^r(x) = \frac{\|x\|^2}{2}$ for $x \in \mathbb{R}^D$, i.e., convex functions ψ^l, ψ^r are congruent w.r.t. weights $(\beta, 1-\beta)$.



Figure 3: The production of **Ave, celeba!** dataset. The 1st line shows images $x \sim \mathbb{P}_{\text{Celeba}}$. Each of 3 next lines shows OT maps $\nabla\psi_n(x) \sim \nabla\psi_n \# \mathbb{P}_{\text{Celeba}} = \mathbb{P}_n$ to constructed measures \mathbb{P}_n . Their barycenter w.r.t. $(\alpha_1, \alpha_2, \alpha_3) = (\frac{1}{4}, \frac{1}{2}, \frac{1}{4})$ is $\mathbb{P}_{\text{Celeba}}$. The last line shows congruence of ψ_n , i.e., $\sum_{n=1}^N \alpha_n \nabla\psi_n(x) \equiv x$. Samples in green boxes are included to dataset.

Besides, for all $x \in \mathbb{R}^D$ the gradient $y^l \stackrel{\text{def}}{=} \nabla\psi^l(x)$ can be computed via solving β -strongly concave optimization:

$$y^l = \arg \max_{y \in \mathbb{R}} \left(\langle x, y \rangle - \beta \frac{\|y\|^2}{2} - (1 - \beta)\psi(y) \right). \quad (12)$$

In turn, the value $y^r \stackrel{\text{def}}{=} \nabla\psi^r(x)$ is given by $y^r = \nabla\psi(y^l)$.

The proof is given in Appendix A. We visualize the idea of our Lemma 2 in Figure 7a. Thanks to Lemma 2, any analytically known convex ψ , e.g., an ICNN, can be used to produce a congruent pair ψ^l, ψ^r . To compute the gradient maps, optimization (12) can be solved by convex optimization tools with $\nabla\psi$ computed by automatic differentiation.

Lemma 3 (Constructing N congruent functions.). *Let $\psi_1^0, \dots, \psi_M^0$ be convex functions, $\beta_1, \dots, \beta_M \in (0, 1)$ and ψ_m^l, ψ_m^r be β_m -left, β_m -right functions for ψ_m^0 respectively. Let $\gamma^l, \gamma^r \in \mathbb{R}^{N \times M}$ be two rectangular matrices with non-negative elements and the sum of elements in each column equals to 1. Let $w_1, \dots, w_M > 0$ satisfy $\sum_{m=1}^M w_m = 1$. For $n = 1, \dots, N$ define*

$$\psi_n(x) \stackrel{\text{def}}{=} \frac{\sum_{m=1}^M w_m [\beta_m \gamma_{nm}^l \psi_m^l(x) + (1 - \beta_m) \gamma_{nm}^r \psi_m^r(x)]}{\sum_{m=1}^M w_m [\beta_m \gamma_{nm}^l + (1 - \beta_m) \gamma_{nm}^r]}. \quad (13)$$

Then ψ_1, \dots, ψ_N are congruent w.r.t. weights

$$\alpha_n \stackrel{\text{def}}{=} \sum_{m=1}^M w_m [\beta_m \gamma_{nm}^l + (1 - \beta_m) \gamma_{nm}^r].$$

We prove Lemma 3 in Appendix A. We visualize the idea of our Lemma 3 in Figure 7b. The lemma provides an elegant way to create $N \geq 2$ congruent functions from convex linear combinations of functions in given congruent pairs (ψ_m^l, ψ_m^r) . Gradients $\nabla\psi_n$ of these functions are respective linear combinations of gradients $\nabla\psi_m^l$ and $\nabla\psi_m^r$.

6. Evaluation

Dataset creation. We use CelebA 64×64 faces dataset (Liu et al., 2015) as the basis for our Ave, celeba! dataset. We assume that CelebA dataset is an empirical sample from the continuous measure $\mathbb{P}_{\text{Celeba}} \in \mathcal{P}_{2,ac}^+(\mathbb{R}^{3 \times 64 \times 64})$ which we put to be the barycenter in our design, i.e., $\bar{\mathbb{P}} = \mathbb{P}_{\text{Celeba}}$. We construct differentiable congruent ψ_n with bijective gradients that produce $\mathbb{P}_n = \nabla\psi_n \# \bar{\mathbb{P}} \in \mathcal{P}_{2,ac}^+(\mathbb{R}^{3 \times 64 \times 64})$ whose unique barycenter is $\mathbb{P}_{\text{Celeba}}$. In Lemma 3, we set $N = 3$, $M = 2$, $\beta_1 = \beta_2 = \frac{1}{2}$, $w_1 = w_2 = \frac{1}{2}$ and

$$(\gamma^l)^\top = \begin{pmatrix} 1 & 0 & 0 \\ 0 & 1 & 0 \end{pmatrix}, \quad (\gamma^r)^\top = \begin{pmatrix} 0 & 1 & 0 \\ 0 & 0 & 1 \end{pmatrix}$$

which yields weights $(\alpha_1, \alpha_2, \alpha_3) = (\frac{1}{4}, \frac{1}{2}, \frac{1}{4})$. We choose the constants above manually to make sure the final produced measures \mathbb{P}_n are visually distinguishable. We use $\psi_m^0(x) = \text{ICNN}_m(s_m(\sigma_m(d_m(x)))) + \lambda \frac{\|x\|^2}{2}$ as convex functions, where ICNNs have ConvICNN64 architecture (Korotin et al., 2021b, Appendix B.1), σ_1, σ_2 are random permutations of pixels and channels, s_1, s_2 are axis-wise random reflections, $\lambda = \frac{1}{100}$. In both functions, d_m is a de-colorization transform which sets R, G, B channels of each pixel to $(\frac{7}{10}R + \frac{1}{25}G + \frac{13}{50}B)$ for ψ_1^0 and $\frac{1}{3}(R+G+B)$ for ψ_2^0 . The weights of ICNNs are initialized by the pre-trained potentials of \mathbb{W}_2^2 "Early" transport benchmark which map blurry faces to the clean ones (Korotin et al., 2021b, §4.1). All the implementation details are given in Appendix B.1.

Finally, to create Ave, celeba! dataset, we randomly split the images dataset into 3 equal parts containing $\approx 67K$ samples, and map each part to respective measure $\mathbb{P}_n = \nabla\psi_n \# \mathbb{P}_{\text{Celeba}}$ by $\nabla\psi_n$. Resulting $3 \times 67K$ samples form the dataset consisting of 3 parts. We show the samples in Figure 3. The samples from the respective parts are in green boxes.

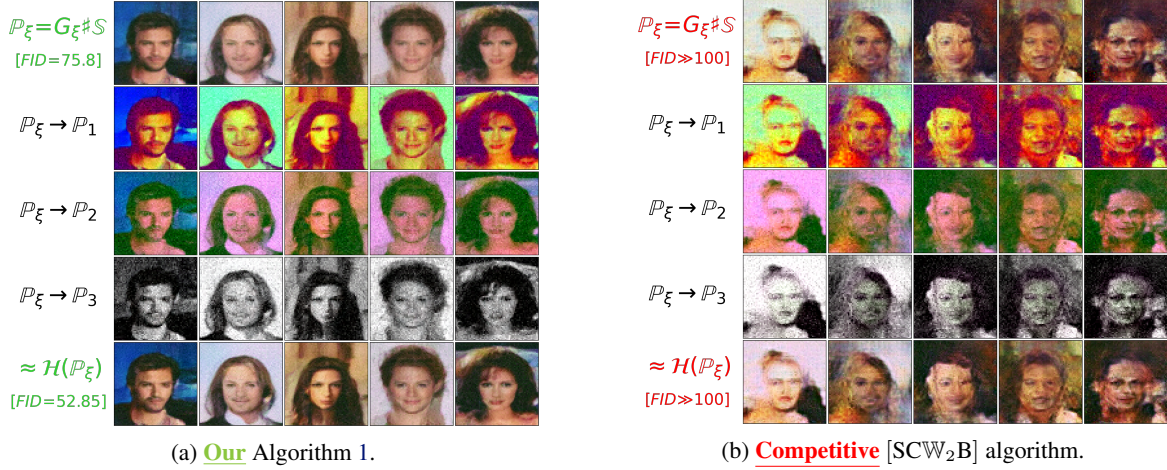


Figure 4: The barycenter and maps to input measures estimated by barycenter algorithms. The 1st line shows generated samples $\mathbb{P}_\xi = G_\xi \# \mathbb{S} \approx \mathbb{P}_{\text{Celeba}}$. Lines 2-4 show maps $\hat{T}_{\mathbb{P}_\xi \rightarrow \mathbb{P}_n}$. The last line shows the average map $\sum_{n=1}^N \alpha_n \hat{T}_{\mathbb{P}_\xi \rightarrow \mathbb{P}_n}$.

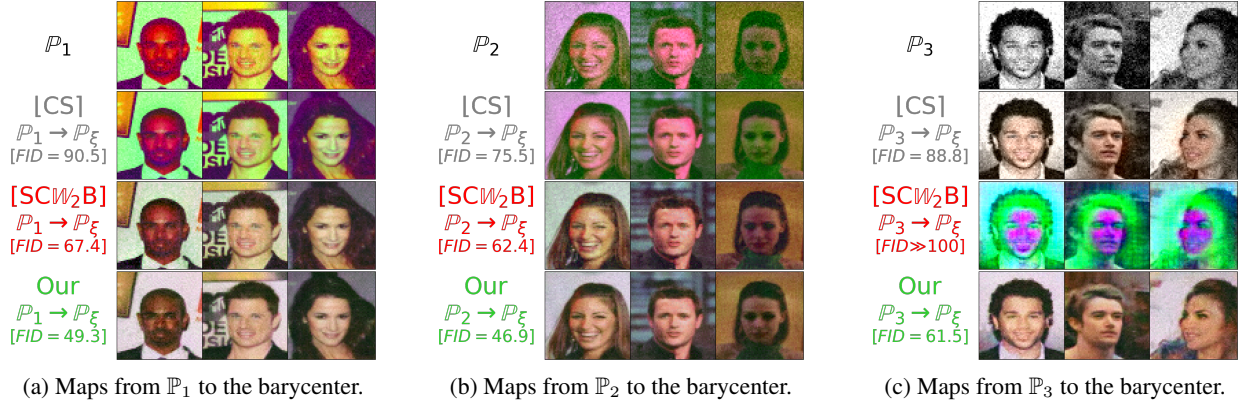


Figure 5: Maps from input measures \mathbb{P}_n ($n = 1, 2, 3$) to the barycenter $\bar{\mathbb{P}}$ estimated by the barycenter algorithms in view. For comparison with the original barycenter images, the faces are the same as in Figure 3.

The code is written on the PyTorch and includes the script for producing Ave, celeba! dataset. The experiments are conducted on 4×GPU GTX 1080ti. Implementation details, architectures and hyperparameters are given in Appendix B.

6.1. Evaluation on Ave, celeba! Dataset

We evaluate our *iterative* algorithm 1 and a recent *variational* [SCW₂B] by (Fan et al., 2020) on Ave, celeba! dataset. Both algorithms use a generative model $\mathbb{P}_\xi = G_\xi \# \mathbb{S}$ for the barycenter and yield approximate maps $\hat{T}_{\mathbb{P}_\xi \rightarrow \mathbb{P}_n}$ to input measures. In our case, the maps are neural networks T_{θ_n} , while in [SCW₂B] they are gradients of ICNNs.

The barycenters of Ave, celeba! fitted by our algorithm and [SCW₂B] are shown in Figures 4a and 4b respectively. Recall the ground truth barycenter is $\mathbb{P}_{\text{Celeba}}$. Thus, for quantitative evaluation we use FID score (Heusel et al., 2017) computed on 200K generated samples w.r.t. the original CelebA dataset, see Table 1. Our method *drastically* outperforms [SCW₂B]. Presumably, this is due to the latter using

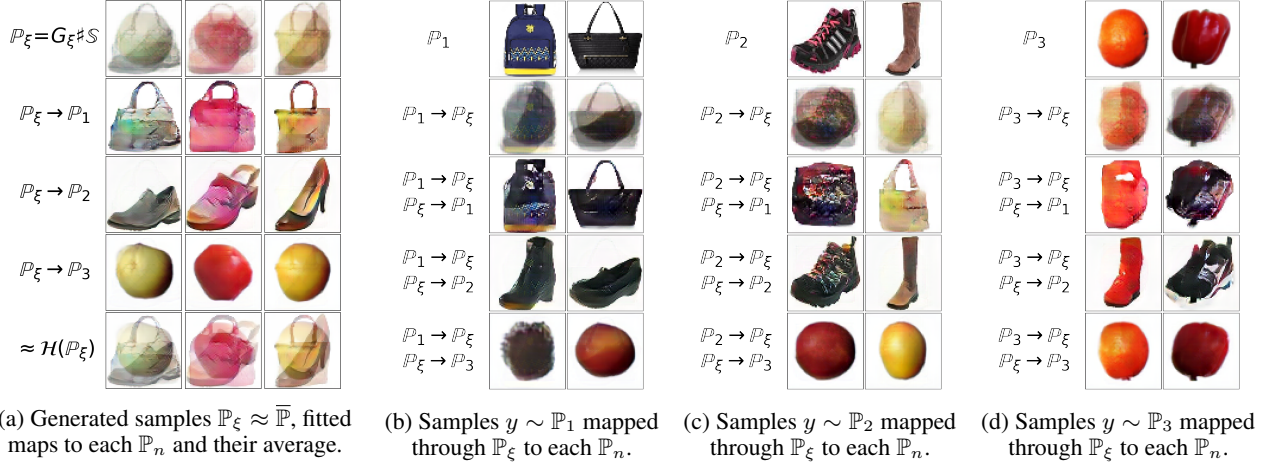
ICNNs which do not provide sufficient performance.

Additionally, we evaluate to which extent the algorithms allow to recover the inverse OT maps $T_{\mathbb{P}_n \rightarrow \mathbb{P}_\xi}$ from inputs \mathbb{P}_n to the barycenter $\mathbb{P}_\xi \approx \bar{\mathbb{P}}$. In [SCW₂B], these maps are computed during training. Our algorithm does not compute them. Thus, we separately fit the inverse maps after main training by using [MM:R] solver between each input \mathbb{P}_n and learned \mathbb{P}_ξ (Algorithm 2 of Appendix 2). The inverse maps are given in Figure 5; their FID scores – in Table 2.

Here we add an additional *constant shift* [CS] baseline which simply shifts the mean of input \mathbb{P}_n to the mean $\bar{\mu}$ of $\bar{\mathbb{P}}$. The vector $\bar{\mu}$ is given by $\sum_{n=1}^N \alpha_n \mu_n$, where μ_n is the mean of \mathbb{P}_n (Álvarez-Esteban et al., 2016). We empirically estimate $\bar{\mu}$ from input samples $y \sim \mathbb{P}_n$.

6.2. Additional Experimental Results

Different domains. To stress-test our algorithm 1, we compute the barycenters w.r.t. $(\alpha_1, \alpha_2, \alpha_3) = (\frac{1}{3}, \frac{1}{3}, \frac{1}{3})$ of notably different datasets: 50K Shoes (Yu & Grauman,


 Figure 6: The barycenter of Handbags, Shoes, Fruit (64×64) datasets fitted by our Algorithm 1.

Method		FID↓
[SCW ₂ B]	$G_\xi(z)$	156.3
	$\sum_{n=1}^N \alpha_n \hat{T}_{\mathbb{P}_\xi \rightarrow \mathbb{P}_n}(G_\xi(z))$	152.1
Ours	$G_\xi(z)$	75.8
	$\sum_{n=1}^N \alpha_n \hat{T}_{\mathbb{P}_\xi \rightarrow \mathbb{P}_n}(G_\xi(z))$	52.85

Table 1: FID scores of images from the learned barycenter.

Method		FID↓		
		$n = 1$	$n = 2$	$n = 3$
[CS]	$y + (\bar{\mu} - \mu_n)$	90.5	75.5	88.8
[SCW ₂ B]	$\hat{T}_{\mathbb{P}_n \rightarrow \mathbb{P}_\xi}(y)$	67.4	62.4	319.62
Ours	$\hat{T}_{\mathbb{P}_n \rightarrow \mathbb{P}_\xi}(y)$	49.3	46.9	61.5

 Table 2: FID scores of images mapped from inputs \mathbb{P}_n .

2014), 138K Amazon Handbags and 90K Fruits (Mureşan & Oltean, 2017). All the images are rescaled to 64×64 .

The ground truth barycenter is unknown, but one may imagine what it looks like. Due to (6), each barycenter image is a pixel-wise average of a shoe, a handbag and a fruit. Our algorithm indeed outputs such a result, see Figure 6. We also show the maps between datasets *through* the barycenter. We provide more examples in Figure 12 of Appendix C.4.

Extra results. In Appendix C.1, we provide *quantitative* results for computing barycenters in the Gaussian case. In Appendix C.2, we test how our algorithm works as a *generative model* on the original CelebA dataset, i.e., when $N = 1$ and $\mathbb{P}_1 = \mathbb{P}_{\text{CelebA}}$. We show that in this case it achieves FID scores comparable to recent WGAN models. In Appendix C.3, similar to (Fan et al., 2020), we compute barycenters of digit classes 0/1 of 32×32 grayscale MNIST (LeCun & Cortes, 2010). We also test our algorithm on FashionMNIST (Xiao et al., 2017) 10 classes dataset.

7. Discussion

Potential impact. We present a scalable barycenter algorithm based on fixed-point iterations with many application

prospects. For instance, in medical imaging, MRI is often acquired at multiple sites where the overlap of information (imaging, genetic, diagnosis) between any two sites is limited. Consequently, the data on each site may be biased and can cause generalizability and robustness issues when training models. The developed algorithm could help to aggregate data from multiple sites and overcome the distributional shift issue across sites.

We expect our Ave, celeba! to become a standard dataset for evaluating continuous barycenter algorithms. In addition, we describe a generic recipe (§5) to produce new datasets.

Limitations. During our fixed-point iterations, the barycenter objective (5) decreases. However, there is no guarantee that the sequence of measures converges to a fixed point or the fixed point is the barycenter. Identifying the precise conditions on the input measures and the initial point is an important future direction. Besides, our algorithm does not recover inverse OT maps $T_{\mathbb{P}_\xi \rightarrow \bar{\mathbb{P}}}$; we compute them with an OT solver as a follow-up. To avoid this second step, one may consider using invertible neural networks (Etmann et al., 2020) to parametrize maps T_{θ_n} in our Algorithm 1.

To create Ave, celeba! dataset (§5), we compose ICNNs with decolorization, random reflections and permutations to simulate degraded images. It is unclear how to produce other practically interesting effects via ICNNs. Studying how to generate more realistic barycenter benchmark is an interesting direction for the future work that will provide insights for benchmarking other OT problems.

References

- Agueh, M. and Carlier, G. Barycenters in the Wasserstein space. *SIAM Journal on Mathematical Analysis*, 43(2): 904–924, 2011.
- Altschuler, J. M., Chewi, S., Gerber, P., and Stromme, A. J.

- Averaging on the bures-wasserstein manifold: dimension-free convergence of gradient descent. *arXiv preprint arXiv:2106.08502*, 2021.
- Álvarez-Esteban, P. C., Del Barrio, E., Cuesta-Albertos, J., and Matrán, C. A fixed-point approach to barycenters in Wasserstein space. *Journal of Mathematical Analysis and Applications*, 441(2):744–762, 2016.
- Amos, B., Xu, L., and Kolter, J. Z. Input convex neural networks. In *Proceedings of the 34th International Conference on Machine Learning-Volume 70*, pp. 146–155. JMLR. org, 2017.
- Arjovsky, M., Chintala, S., and Bottou, L. Wasserstein GAN. *arXiv preprint arXiv:1701.07875*, 2017.
- Bespalov, I., Buzun, N., Kachan, O., and Dylov, D. V. Data augmentation with manifold barycenters. *arXiv preprint arXiv:2104.00925*, 2021.
- Bigot, J., Cazelles, E., and Papadakis, N. Data-driven regularization of wasserstein barycenters with an application to multivariate density registration. *Information and Inference: A Journal of the IMA*, 8(4):719–755, 2019.
- Bonneel, N., Rabin, J., Peyré, G., and Pfister, H. Sliced and radon wasserstein barycenters of measures. *Journal of Mathematical Imaging and Vision*, 51(1):22–45, 2015.
- Brenier, Y. Polar factorization and monotone rearrangement of vector-valued functions. *Communications on pure and applied mathematics*, 44(4):375–417, 1991.
- Chen, Y., Telgarsky, M., Zhang, C., Bailey, B., Hsu, D., and Peng, J. A gradual, semi-discrete approach to generative network training via explicit Wasserstein minimization. In *International Conference on Machine Learning*, pp. 1071–1080. PMLR, 2019.
- Chewi, S., Maunu, T., Rigollet, P., and Stromme, A. J. Gradient descent algorithms for bures-wasserstein barycenters. In *Conference on Learning Theory*, pp. 1276–1304. PMLR, 2020.
- Colombo, P., Staerman, G., Clavel, C., and Piantanida, P. Automatic text evaluation through the lens of wasserstein barycenters, 2021.
- Dognin, P., Melnyk, I., Mroueh, Y., Ross, J., Santos, C. D., and Sercu, T. Wasserstein barycenter model ensembling. *arXiv preprint arXiv:1902.04999*, 2019.
- Etmann, C., Ke, R., and Schönlieb, C.-B. iunets: learnable invertible up-and downsampling for large-scale inverse problems. In *2020 IEEE 30th International Workshop on Machine Learning for Signal Processing (MLSP)*, pp. 1–6. IEEE, 2020.
- Fan, J., Taghvaei, A., and Chen, Y. Scalable computations of Wasserstein barycenter via input convex neural networks. *arXiv preprint arXiv:2007.04462*, 2020.
- Fenchel, W. On conjugate convex functions. *Canadian Journal of Mathematics*, 1(1):73–77, 1949.
- Genevay, A., Cuturi, M., Peyré, G., and Bach, F. Stochastic optimization for large-scale optimal transport. In *Advances in neural information processing systems*, pp. 3440–3448, 2016.
- Genevay, A., Peyré, G., and Cuturi, M. Gan and vae from an optimal transport point of view. *arXiv preprint arXiv:1706.01807*, 2017.
- Heusel, M., Ramsauer, H., Unterthiner, T., Nessler, B., and Hochreiter, S. GANs trained by a two time-scale update rule converge to a local nash equilibrium. In *Advances in neural information processing systems*, pp. 6626–6637, 2017.
- Inouye, D. I., Zhou, Z., Gong, Z., and Ravikumar, P. Iterative barycenter flows. *arXiv preprint arXiv:2104.07232*, 2021.
- Kantorovitch, L. On the translocation of masses. *Management Science*, 5(1):1–4, 1958.
- Kingma, D. P. and Ba, J. Adam: A method for stochastic optimization. *arXiv preprint arXiv:1412.6980*, 2014.
- Korotin, A., Egiazarian, V., Asadulaev, A., Safin, A., and Burnaev, E. Wasserstein-2 generative networks. In *International Conference on Learning Representations*, 2021a. URL https://openreview.net/forum?id=bEoxzW_EXsa.
- Korotin, A., Li, L., Genevay, A., Solomon, J., Filippov, A., and Burnaev, E. Do neural optimal transport solvers work? a continuous wasserstein-2 benchmark. *arXiv preprint arXiv:2106.01954*, 2021b.
- Korotin, A., Li, L., Solomon, J., and Burnaev, E. Continuous wasserstein-2 barycenter estimation without minimax optimization. In *International Conference on Learning Representations*, 2021c. URL <https://openreview.net/forum?id=3tFAs5E-Pe>.
- Korotin, A., V’yugin, V., and Burnaev, E. Mixability of integral losses: A key to efficient online aggregation of functional and probabilistic forecasts. *Pattern Recognition*, 120:108175, 2021d.
- Lacombe, J., Digne, J., Courty, N., and Bonneel, N. Learning to generate wasserstein barycenters. *arXiv preprint arXiv:2102.12178*, 2021.

- LeCun, Y. and Cortes, C. MNIST handwritten digit database. 2010. URL <http://yann.lecun.com/exdb/mnist/>.
- Li, L., Genevay, A., Yurochkin, M., and Solomon, J. Continuous regularized Wasserstein barycenters. *arXiv preprint arXiv:2008.12534*, 2020.
- Liu, H., Gu, X., and Samaras, D. Wasserstein GAN with quadratic transport cost. In *Proceedings of the IEEE International Conference on Computer Vision*, pp. 4832–4841, 2019.
- Liu, Z., Luo, P., Wang, X., and Tang, X. Deep learning face attributes in the wild. In *Proceedings of International Conference on Computer Vision (ICCV)*, December 2015.
- Lu, G., Zhou, Z., Shen, J., Chen, C., Zhang, W., and Yu, Y. Large-scale optimal transport via adversarial training with cycle-consistency. *arXiv preprint arXiv:2003.06635*, 2020.
- Lucic, M., Kurach, K., Michalski, M., Gelly, S., and Bousquet, O. Are GANs created equal? a large-scale study. In *Advances in neural information processing systems*, pp. 700–709, 2018.
- Lyu, B., Nguyen, T., Ishwar, P., Scheutz, M., and Aeron, S. Barycentric distribution alignment and manifold-restricted invertibility for domain generalization, 2021.
- Makkuva, A. V., Taghvaei, A., Oh, S., and Lee, J. D. Optimal transport mapping via input convex neural networks. *arXiv preprint arXiv:1908.10962*, 2019.
- Metelli, A. M., Likmeta, A., and Restelli, M. Propagating uncertainty in reinforcement learning via wasserstein barycenters. In *33rd Conference on Neural Information Processing Systems, NeurIPS 2019*, pp. 4335–4347. Curran Associates, Inc., 2019.
- Mokrov, P., Korotin, A., Li, L., Genevay, A., Solomon, J., and Burnaev, E. Large-scale wasserstein gradient flows. *arXiv preprint arXiv:2106.00736*, 2021.
- Montesuma, E. F. and Mboula, F. M. N. Wasserstein barycenter for multi-source domain adaptation. In *Proceedings of the IEEE/CVF Conference on Computer Vision and Pattern Recognition*, pp. 16785–16793, 2021.
- Mroueh, Y. Wasserstein style transfer. *arXiv preprint arXiv:1905.12828*, 2019.
- Mureşan, H. and Oltean, M. Fruit recognition from images using deep learning. *arXiv preprint arXiv:1712.00580*, 2017.
- Nhan Dam, Q. H., Le, T., Nguyen, T. D., Bui, H., and Phung, D. Threeplayer Wasserstein GAN via amortised duality. In *Proc. of the 28th Int. Joint Conf. on Artificial Intelligence (IJCAI)*, 2019.
- Paris, Q. Online learning with exponential weights in metric spaces. *arXiv preprint arXiv:2103.14389*, 2021.
- Peyré, G., Cuturi, M., et al. Computational optimal transport. *Foundations and Trends® in Machine Learning*, 11(5-6): 355–607, 2019.
- Rabin, J., Peyré, G., Delon, J., and Bernot, M. Wasserstein barycenter and its application to texture mixing. In *International Conference on Scale Space and Variational Methods in Computer Vision*, pp. 435–446. Springer, 2011.
- Rabin, J., Ferradans, S., and Papadakis, N. Adaptive color transfer with relaxed optimal transport. In *2014 IEEE International Conference on Image Processing (ICIP)*, pp. 4852–4856. IEEE, 2014.
- Rockafellar, R. T. Integral functionals, normal integrands and measurable selections. In *Nonlinear operators and the calculus of variations*, pp. 157–207. Springer, 1976.
- Ronneberger, O., Fischer, P., and Brox, T. U-net: Convolutional networks for biomedical image segmentation. In *International Conference on Medical image computing and computer-assisted intervention*, pp. 234–241. Springer, 2015.
- Rout, L., Korotin, A., and Burnaev, E. Generative modeling with optimal transport maps. *arXiv preprint arXiv:2110.02999*, 2021.
- Santambrogio, F. Optimal transport for applied mathematicians. *Birkhäuser, NY*, 55(58-63):94, 2015.
- Seguy, V., Damodaran, B. B., Flamary, R., Courty, N., Rolet, A., and Blondel, M. Large-scale optimal transport and mapping estimation. *arXiv preprint arXiv:1711.02283*, 2017.
- Simon, D. and Aberdam, A. Barycenters of natural images constrained wasserstein barycenters for image morphing. In *Proceedings of the IEEE/CVF Conference on Computer Vision and Pattern Recognition*, pp. 7910–7919, 2020.
- Simonyan, K. and Zisserman, A. Very deep convolutional networks for large-scale image recognition. *arXiv preprint arXiv:1409.1556*, 2014.
- Solomon, J., De Goes, F., Peyré, G., Cuturi, M., Butscher, A., Nguyen, A., Du, T., and Guibas, L. Convolutional Wasserstein distances: Efficient optimal transportation

- on geometric domains. *ACM Transactions on Graphics (TOG)*, 34(4):1–11, 2015.
- Srivastava, S., Cevher, V., Dinh, Q., and Dunson, D. Wasp: Scalable bayes via barycenters of subset posteriors. In *Artificial Intelligence and Statistics*, pp. 912–920, 2015.
- Srivastava, S., Li, C., and Dunson, D. B. Scalable bayes via barycenter in Wasserstein space. *The Journal of Machine Learning Research*, 19(1):312–346, 2018.
- Staudt, T., Hundrieser, S., and Munk, A. On the uniqueness of kantorovich potentials. *arXiv preprint arXiv:2201.08316*, 2022.
- Taghvaei, A. and Jalali, A. 2-Wasserstein approximation via restricted convex potentials with application to improved training for GANs. *arXiv preprint arXiv:1902.07197*, 2019.
- Villani, C. *Topics in optimal transportation*. Number 58. American Mathematical Soc., 2003.
- Villani, C. *Optimal transport: old and new*, volume 338. Springer Science & Business Media, 2008.
- Xiao, H., Rasul, K., and Vollgraf, R. Fashion-mnist: a novel image dataset for benchmarking machine learning algorithms. *arXiv preprint arXiv:1708.07747*, 2017.
- Xie, Y., Chen, M., Jiang, H., Zhao, T., and Zha, H. On scalable and efficient computation of large scale optimal transport. volume 97 of *Proceedings of Machine Learning Research*, pp. 6882–6892, Long Beach, California, USA, 09–15 Jun 2019. PMLR. URL <http://proceedings.mlr.press/v97/xie19a.html>.
- Yu, A. and Grauman, K. Fine-grained visual comparisons with local learning. In *Proceedings of the IEEE Conference on Computer Vision and Pattern Recognition*, pp. 192–199, 2014.

A. Proofs

First, we recall basic properties of convex conjugate functions that we rely on in our proofs. Let $\psi : \mathbb{R}^D \rightarrow \mathbb{R}$ be a convex function and $\bar{\psi}$ be its convex conjugate. From the definition of $\bar{\psi}$, we obtain

$$\psi(x) + \bar{\psi}(y) \geq \langle x, y \rangle$$

for all $x, y \in \mathbb{R}^D$. Assume that ψ is differentiable and has an invertible gradient $\nabla\psi : \mathbb{R}^D \rightarrow \mathbb{R}^D$. The latter condition holds, e.g., for strongly convex functions. From the convexity of ψ , we derive

$$x = \arg \max_{x \in \mathbb{R}^D} [\langle x, y \rangle - \psi(x)] \Leftrightarrow y = \nabla\psi(x) \Leftrightarrow x = (\nabla\psi)^{-1}(y),$$

which yields

$$\bar{\psi}(y) = \langle (\nabla\psi)^{-1}(x), x \rangle - \psi((\nabla\psi)^{-1}(x)).$$

In particular, the strict equality $\psi(x) + \bar{\psi}(y) = \langle x, y \rangle$ holds if and only if $y = \nabla\psi(x)$. By applying the same logic to $\bar{\psi}$, we obtain $(\nabla\bar{\psi})^{-1} = \nabla\psi$ and $(\nabla\psi)^{-1} = \nabla\bar{\psi}$, i.e., the gradients of conjugate functions are mutually inverse.

A.1. Proof of Lemma 1

Proof. For each $n = 1, 2, \dots, N$ we perform the following evaluation:

$$\frac{\partial}{\partial \xi} \mathbb{W}_2^2(G_\xi \# \mathbb{S}, \mathbb{P}_n) = \int_z \mathbf{J}_\xi G_\xi(z)^T \nabla u_n^*(G_\xi(z)) d\mathbb{S}(z), = \int_z \mathbf{J}_\xi G_\xi(z)^T (G_\xi(z) - T_{\mathbb{P}_\xi \rightarrow \mathbb{P}_n}(G_\xi(z))) d\mathbb{S}(z), \quad (14)$$

where u_n^* is the optimal dual potential for $\mathbb{P}_\xi = G_\xi \# \mathbb{S}$ and \mathbb{P}_n . The first equation in (14) follows from (Genevay et al., 2017, Equation 3). The second equation in (14) follows from the property $\nabla u_n^*(x) = x - T_{\mathbb{P}_\xi \rightarrow \mathbb{P}_n}(x)$ connecting dual potentials and OT maps.

We sum (14) for $n = 1, \dots, N$ w.r.t. weights α_n with $\xi = \xi_0$ and obtain

$$\frac{\partial}{\partial \xi} \sum_{n=1}^N \alpha_n \mathbb{W}_2^2(G_\xi \# \mathbb{S}, \mathbb{P}_n) = \int_z \mathbf{J}_\xi G_{\xi_0}(z)^T \left(G_{\xi_0}(z) - \sum_{n=1}^N \alpha_n T_{\mathbb{P}_{\xi_0} \rightarrow \mathbb{P}_n}(G_{\xi_0}(z)) \right) d\mathbb{S}(z). \quad (15)$$

The last step is to note that (15) exactly matches the derivative of the left-hand side of (10) evaluated at $\xi = \xi_0$. □

A.2. Proof of Lemma 2

Proof. First, we prove the congruence, i.e., $\beta\psi^l(x) + (1 - \beta)\psi^r(x) = \frac{\|x\|^2}{2}$ for all $x \in \mathbb{R}^D$.

$$\begin{aligned} & \beta\psi^l(x) + (1 - \beta)\psi^r(x) = \\ & \beta \max_{y_1 \in \mathbb{R}^D} [\langle x, y_1 \rangle - \bar{\psi}^l(y_1)] + (1 - \beta) \max_{y_2 \in \mathbb{R}^D} [\langle x, y_2 \rangle - \bar{\psi}^r(y_2)] = \end{aligned} \quad (16)$$

$$\begin{aligned} & \beta \max_{y_1 \in \mathbb{R}^D} [\langle x, y_1 \rangle - \beta \frac{\|y_1\|^2}{2} - (1 - \beta)\psi(y_1)] + \\ & (1 - \beta) \max_{y_2 \in \mathbb{R}^D} [\langle x, y_2 \rangle - (1 - \beta) \frac{\|y_2\|^2}{2} - \beta\bar{\psi}(x)] = \\ & \max_{y_1, y_2 \in \mathbb{R}^D} [\langle x, \beta y_1 + (1 - \beta)y_2 \rangle - \beta^2 \frac{\|y_1\|^2}{2} - (1 - \beta)^2 \frac{\|y_2\|^2}{2} - \beta(1 - \beta)(\psi(y_1) + \bar{\psi}(y_2))] \leq \end{aligned} \quad (17)$$

$$\begin{aligned} & \max_{y_1, y_2 \in \mathbb{R}^D} [\langle x, \beta y_1 + (1 - \beta)y_2 \rangle - \beta^2 \frac{\|y_1\|^2}{2} - (1 - \beta)^2 \frac{\|y_2\|^2}{2} - \beta(1 - \beta)\langle y_1, y_2 \rangle] = \\ & \max_{y_1, y_2 \in \mathbb{R}^D} \frac{\|x\|^2}{2} - \frac{1}{2} \|x - (\beta y_1 + (1 - \beta)y_2)\|^2 \leq \frac{\|x\|^2}{2}. \end{aligned} \quad (18)$$

First, we substitute $(y_1, y_2) = (y^l, \nabla\psi(y^l))$. For this pair, $x = \nabla\bar{\psi}^l(y^l) = \beta y^l + (1 - \beta)\nabla\psi(y^l)$, which results in $x = \beta y_1 + (1 - \beta)y_2$. Moreover, since $y_2 = \nabla\psi(y_1)$, we have $\psi(y_1) + \bar{\psi}(y_2) = \langle y_1, y_2 \rangle$. As the consequence, both inequalities (17) and (18) turn to strict equalities yielding congruence of ψ^l, ψ^r .

From (11), the smoothness and strong convexity of ψ imply that ψ^l and ψ^r are smooth. Consequently, $\overline{\psi^l}$ and $\overline{\psi^r}$ are strongly convex. Thus, the maximizer of (16) is unique. We know the maximum of (16) is attained at $(y_1, y_2) = (\nabla \psi^l(x), \nabla \psi^r(x)) = (y^l, y^r)$. We conclude $(y^l, y^r) = (y^l, \nabla \psi(y^l))$, i.e., $y^r = \nabla \psi(y^l)$. Finally, $y^l = \nabla \psi^l(x) \Leftrightarrow x = \nabla \overline{\psi^l}(y^l) \Leftrightarrow y^l = \max_{y \in \mathbb{R}^D} [\langle x, y \rangle - \overline{\psi^l}(y)]$, which matches (12). \square

A.3. Proof of Lemma 3

Proof. First, we check that $\sum_{n=1}^N \alpha_n$ indeed equals 1:

$$\begin{aligned} \sum_{n=1}^N \alpha_n &= \sum_{n=1}^N \sum_{m=1}^M w_m [\beta_m \gamma_{nm}^l + (1 - \beta_m) \gamma_{nm}^r] = \sum_{m=1}^M [w_m \beta_m \underbrace{\sum_{n=1}^N \gamma_{nm}^l}_{=1}] + \sum_{m=1}^M [w_m (1 - \beta_m) \underbrace{\sum_{n=1}^N \gamma_{nm}^r}_{=1}] = \\ &= \sum_{m=1}^M w_m \beta_m + \sum_{m=1}^M w_m (1 - \beta_m) = \sum_{m=1}^M w_m (\beta_m + (1 - \beta_m)) = \sum_{m=1}^M w_m = 1. \end{aligned} \quad (19)$$

Next, we check that ψ_1, \dots, ψ_N are congruent w.r.t. weights $\alpha_1, \dots, \alpha_N$:

$$\begin{aligned} \sum_{n=1}^N \alpha_n \psi_n(x) &= \sum_{n=1}^N \sum_{m=1}^M w_m [\beta_m \gamma_{nm}^l \cdot \psi_m^l(x) + (1 - \beta_m) \gamma_{nm}^r \cdot \psi_m^r(x)] = \\ &= \sum_{m=1}^M [w_m \beta_m \underbrace{\psi_m^l(x) \sum_{n=1}^N \gamma_{nm}^l}_{=1}] + \sum_{m=1}^M [w_m (1 - \beta_m) \underbrace{\psi_m^r(x) \sum_{n=1}^N \gamma_{nm}^r}_{=1}] = \\ &= \sum_{m=1}^M [w_m \underbrace{(\beta_m \psi_m^l(x) + (1 - \beta_m) \psi_m^r(x))}_{= \frac{\|x\|^2}{2}}] = \sum_{m=1}^M w_m \frac{\|x\|^2}{2} = \frac{\|x\|^2}{2}. \end{aligned}$$

\square

B. Experimental Details

B.1. Ave, celeba! Dataset Creation

The initialization of random permutations σ_m and reflections s_m (for $m = 1, 2$) as well as the random split of CelebA dataset into 3 parts (each containing $\approx 67K$ images) are *hardcoded* in our provided script for producing Ave, celeba! dataset. To initialize ICNN $_m$ (for $m = 1, 2$), we use use ConvICNN64 (Korotin et al., 2021b, Appendix B.1) checkpoints Early_v1_conj.pt, Early_v2_conj.pt from the official Wasserstein-2 benchmark repository¹.

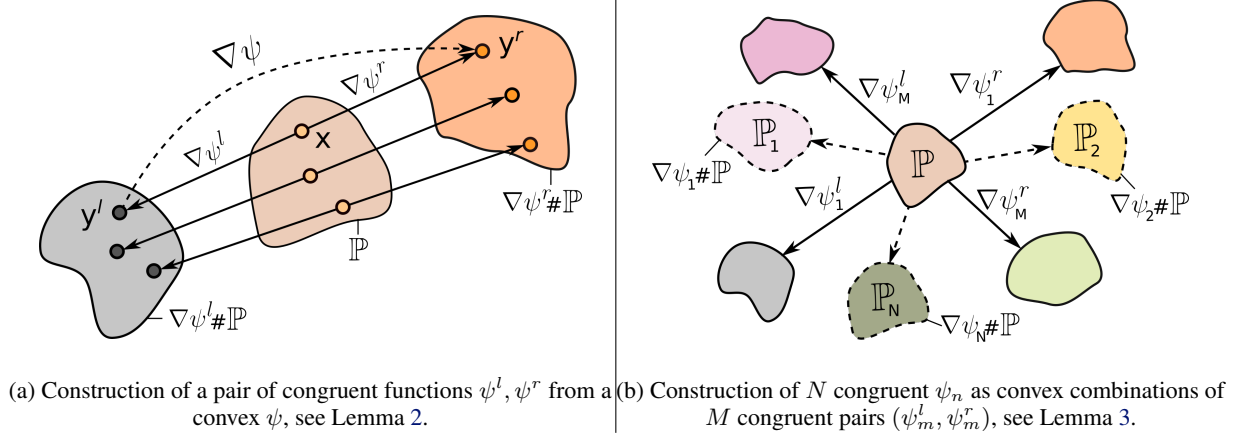
We rescale Celeba images to 64×64 by using `imresize` from `scipy.misc`. To create empirical samples from input distributions \mathbb{P}_n by using the rescaled CelebA dataset, we compute the gradient maps $\nabla \psi_n(x)$ ($n = 1, 2, 3$) in Lemma 3 for images x in the CelebA dataset. This computation implies computing gradient maps $\nabla \psi_m^l(x)$ and $\nabla \psi_m^r(x)$ for each base function ψ_m^0 ($m = 1, 2$) and summing them with respective coefficients (13). Following our Lemma 2, we compute $y_m^l \stackrel{\text{def}}{=} \nabla \psi_m^l(x)$ by solving a concave optimization problem (12) over the space of images. We solve this problem with the gradient descent. We use Adam optimizer (Kingma & Ba, 2014) with default betas, $lr = 2 \cdot 10^{-2}$ and do 1000 gradient steps. To speed up the computation, we simultaneously solve the problem for a batch of 256 images x from CelebA dataset. After the optimization, we compute $y^r \stackrel{\text{def}}{=} \nabla \psi_m^r(x)$ as $y^r = \nabla \psi_m(y^l)$ (Lemma 2).

Computational complexity. The process of producing Ave, celeba! dataset takes about 1, 5 days on a GPU GTX 1080 ti.

B.2. Hyperparameters (Algorithm 1, Main Training)

We provide the hyperparameters of all the experiments with algorithm 1 in Table 3. The column **total iters** shows the sum of gradient steps over generator G_ξ and each of N potentials v_{ω_n} in OT solvers.

¹<https://github.com/iamalexkorotin/Wasserstein2Benchmark>


 Figure 7: Construction of tuples of congruent functions and production of measures with known \mathbb{W}_2 barycenter (§5).

Optimization. We use Adam optimizer with the default betas. During training, we decrease the learning rates of the generator G_ξ and each potential v_{ω_n} every 10K steps of their optimizers. In the Gaussian case, we use a single GPU GTX 1080ti. In all other cases we split the batch over $4 \times \text{GPU GTX 1080ti}$ (`nn.DataParallel` in PyTorch).

Neural Network Architectures. In the Gaussian case, we use In the evaluation in the Gaussian case, we use sequential fully-connected neural networks with ReLU activations for the generator $G_\xi : \mathbb{R}^D \rightarrow \mathbb{R}^D$, potentials $v_{\omega_n} : \mathbb{R}^D \rightarrow \mathbb{R}$ and transport maps $T_{\theta_n} : \mathbb{R}^D \rightarrow \mathbb{R}^D$. For all the networks the sizes of hidden layers are:

$$[\max(100, 2D), \max(100, 2D), \max(100, 2D)].$$

In the experiments with images, we use the ResNet² generator and discriminator architectures of WGAN-QC (Liu et al., 2019) for our generator G_ξ and potentials v_{ω_n} respectively. As the maps T_{θ_n} , we use U-Net³ (Ronneberger et al., 2015).

Generator regression loss. In the Gaussian case and experiments with grayscale images (MNIST, FashionMNIST), we use mean squared loss for generator regression. In other experiments, we use the perceptual mean squared loss based on the features of the pre-trained VGG-16 network (Simonyan & Zisserman, 2014). The loss is hardcoded in the implementation.

Data pre-processing. In all experiments with images we normalize them to $[-1, 1]$. We rescale MNIST and FashionMNIST images to 32×32 . In all other cases, we rescale images to 64×64 . Note that Fruit360 dataset originally contains 114×114 images; before rescaling, we add white color padding to make the images have the size 128×128 . Working with Ave, celeba! dataset, we additionally shift each subset \mathbb{P}_n by $(\bar{\mu} - \mu_n)$, i.e., we train the models on the [CS] baseline. This helps the models to avoid learning the shift.

Computational complexity. The most challenging experiments (Ave, celeba! and Handbags, Shoes, Fruit barycenters) take about 2-3 days to converge on $4 \times \text{GPU GTX 1080 ti}$. Other experiments converge faster.

Experiment	D	H	N	G_ξ	v_{ω_n}	T_{θ_n}	k_G	k_v	k_T	lr_G	lr_v	lr_T	ℓ	Total iters	Batch size
Gaussians	2-128	2-128	4	MLP	MLP				10	$1 \cdot 10^{-4}$	$1 \cdot 10^{-3}$	$1 \cdot 10^{-3}$	MSE	12K	1024
MNIST 0/1	1024	16	2						15	$1 \cdot 10^{-4}$	$1 \cdot 10^{-4}$	$1 \cdot 10^{-4}$		60K	
FashionMNIST			10						10	$1 \cdot 10^{-4}$	$1 \cdot 10^{-4}$	$1 \cdot 10^{-4}$		100K	
Bags, Shoes, Fruit			3						10	$3 \cdot 10^{-4}$	$3 \cdot 10^{-4}$	$3 \cdot 10^{-4}$		36K	
Ave, celeba!			3						10	$3 \cdot 10^{-4}$	$3 \cdot 10^{-4}$	$3 \cdot 10^{-4}$		60K	
Celeba	12288	128	1						15	$1 \cdot 10^{-4}$	$1 \cdot 10^{-4}$	$1 \cdot 10^{-4}$	VGG	80K	
Celeba (fixed G)			1				0		15	$1 \cdot 10^{-4}$	$1 \cdot 10^{-4}$	$1 \cdot 10^{-4}$		120K	

Table 3: Hyperparameters that we use in the experiments with our algorithm 1.

²<https://github.com/harryliu/WGAN-QC>

³<https://github.com/milesial/Pytorch-UNet>

Algorithm 2: Learning maps from input measures to the learned barycenter $\mathbb{P}_\xi \approx \bar{\mathbb{P}}$ with [MM:R] OT solver.

Input : latent \mathbb{S} and input $\mathbb{P}_1, \dots, \mathbb{P}_N$ measures; pretrained generator $G_\xi : \mathbb{R}^H \rightarrow \mathbb{R}^D$ satisfying $G_\xi \# \mathbb{S} \approx \bar{\mathbb{P}}$;
 mapping networks $T_{\theta'_1}^{\text{inv}}, \dots, T_{\theta'_N}^{\text{inv}} : \mathbb{R}^D \rightarrow \mathbb{R}^D$; potentials $v_{\omega'_1}^{\text{inv}}, \dots, v_{\omega'_N}^{\text{inv}} : \mathbb{R}^D \rightarrow \mathbb{R}$;
 number of inner iterations for training transport maps: K_T ;

Output : OT maps satisfying $T_{\theta'_n}^{\text{inv}} \# \mathbb{P}_n \approx \mathbb{P}_\xi = (G_\xi \# \mathbb{S}) \approx \bar{\mathbb{P}}$;

repeat

for $n = 1, 2, \dots, N$ **do**

 Sample batches $Z \sim \mathbb{S}, Y \sim \mathbb{P}_n; X \leftarrow G_\xi(Z)$;
 $\mathcal{L}_v \leftarrow \frac{1}{|Y|} \sum_{y \in Y} v_{\omega'_n}^{\text{inv}}(T_{\theta'_n}^{\text{inv}}(y)) - \frac{1}{|X|} \sum_{x \in X} v_{\omega'_n}^{\text{inv}}(x)$;

 Update ω'_n by using $\frac{\partial \mathcal{L}_v}{\partial \omega'_n}$;

for $k_T = 1, 2, \dots, K_T$ **do**

 Sample batch $Y \sim \mathbb{P}_n$;

$\mathcal{L}_T = \frac{1}{|Y|} \sum_{y \in Y} [\frac{1}{2} \|y - T_{\theta'_n}^{\text{inv}}(y)\|^2 - v_{\omega'_n}^{\text{inv}}(T_{\theta'_n}^{\text{inv}}(y))]$;

 Update θ'_n by using $\frac{\partial \mathcal{L}_T}{\partial \theta'_n}$;

until *not converged*;

B.3. Hyperparameters (Algorithm 2, Learning Maps to the Barycenter)

After using the main algorithm 1 to train G_ξ , we use algorithm 2 to extract the inverse optimal maps $\mathbb{P}_n \rightarrow \mathbb{P}_\xi$. We detail the hyperparameters in Table 4 below. In all the cases we use Adam optimizer with the default betas. The column **total iters** show the number of update steps for each potential $v_{\omega'_n}^{\text{inv}}$.

Experiment	D	N	v_{ω_n}	T_{θ_n}	k_T	lr_v	lr_T	Total iters	Batch size
MNIST 0/1	1024	2	ResNet	UNet	10	$1 \cdot 10^{-4}$	$1 \cdot 10^{-4}$	4k	64
FashionMNIST		10						4k	
Bags, Shoes, Fruit	12288	3						20K	
Ave, celeba!		3						12K	

Table 4: Hyperparameters that we use in the experiments with algorithm 2

B.4. Hyperparameters of competitive [SCW₂B] algorithm

On Ave, celeba! we use (Fan et al., 2020, Algorithm 1) with $k_3 = 50000$, $k_2 = k_1 = 10$. The optimizer, the learning rates and the generator network are the same as in our algorithm. However, for the potentials (OT solver), we use ICNN architecture as it is required by their method. We use ConvICNN64 (Korotin et al., 2021b, Appendix B.1) architecture.

C. Additional Experimental Results

C.1. Gaussian Case

Similar to (Korotin et al., 2021c; Fan et al., 2020), we consider toy Gaussian case for which the true barycenter can be computed (Álvarez-Esteban et al., 2016, §4). We use $N = 4$ measures with weights $(\alpha_1, \dots, \alpha_4) = (\frac{1}{10}, \frac{2}{10}, \frac{3}{10}, \frac{4}{10})$. By using the publicly available code of (Korotin et al., 2021c), we initialize $\mathbb{P}_n = \mathcal{N}(0, S_n^T \Lambda S_n)$, where S_n is a random rotation matrix and Λ is diagonal with entries $[\frac{1}{2}b^0, \frac{1}{2}b^1, \dots, 2]$, where $b = {}^{D-1}\sqrt{4}$. We quantify the generated \mathbb{W}_2 barycenter $G_\xi \# \mathbb{S}$ with the Bures-Wasserstein Unexplained Variance Percentage (Korotin et al., 2021c, §5) metric:

$$\text{BW}_2^2\text{-UVP}(G_\xi \# \mathbb{S}, \bar{\mathbb{P}}) = 100 \cdot \text{BW}_2^2(G_\xi \# \mathbb{S}, \bar{\mathbb{P}}) / [\frac{1}{2} \text{Var}(\bar{\mathbb{P}})] \%,$$

where $\text{BW}_2^2(\mathbb{P}, \mathbb{Q}) = \mathbb{W}_2^2(\mathcal{N}(\mu_{\mathbb{P}}, \Sigma_{\mathbb{P}}), \mathcal{N}(\mu_{\mathbb{Q}}, \Sigma_{\mathbb{Q}}))$ is the Bures-Wasserstein metric and $\mu_{\mathbb{P}}, \Sigma_{\mathbb{P}}$ denote mean and covariance of the measure \mathbb{P} . The metric admits the closed form (Chewi et al., 2020). For the trivial baseline prediction $G_{\xi_0}(z) \equiv \mu_{\bar{\mathbb{P}}} \equiv \sum_{n=1}^N \alpha_n \mu_{\mathbb{P}_n}$ the metric value is 100%. We denote this baseline as $\lfloor C \rfloor$.

Method	D=2	4	8	16	32	64	128
[C]	100	100	100	100	100	100	100
[SCW ₂ B]	0.07	0.09	0.16	0.28	0.43	0.59	1.28
Ours	0.01	0.02	0.01	0.08	0.11	0.23	0.38

 Table 5: Comparison of $\text{BW}_2^2\text{-UVP}\downarrow$ (%) in the Gaussian case.

The results of our algorithm 1 and [SCW₂B] adapted from (Korotin et al., 2021c, Table 1) are given in Table 5. Both algorithms work well in the Gaussian case and provide $\text{BW}_2\text{-UVP} < 2\%$ in dimension 128.

C.2. Generative Modeling

Analogously to (Fan et al., 2020), we evaluate our algorithm when $N = 1$. In this case, the minimizer of (5) is the measure \mathbb{P}_1 itself, i.e., $\bar{\mathbb{P}} = \mathbb{P}_1$. As the result, our algorithm 1 works as a usual generative model, i.e., it fits data \mathbb{P}_1 by a generator G_ξ . For experiments, we use CelebA 64×64 dataset. Generated images $G_\xi(z)$ and $\hat{T}_{\mathbb{P}_\xi \rightarrow \mathbb{P}_1}(G_\xi(z))$ are shown in Figure 8a.

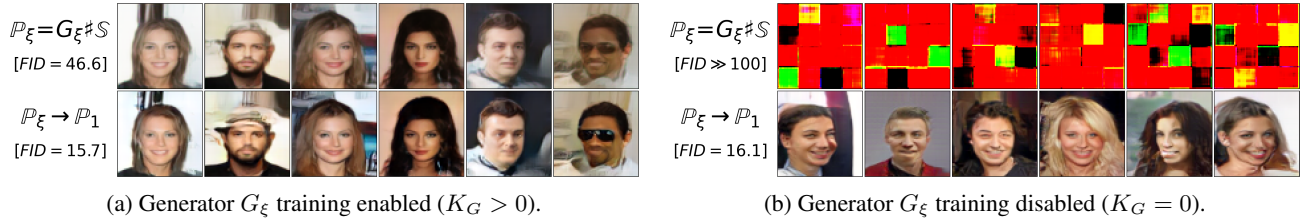


Figure 8: Images generated by our algorithm 1 serving as a generative model. The 1st line shows samples from $G_\xi \# \mathbb{S} \approx \mathbb{P}_1$, the 2nd line shows estimated OT map $\hat{T}_{\mathbb{P}_\xi \rightarrow \mathbb{P}_1}$ from $G_\xi \# \mathbb{S}$ to \mathbb{P}_1 which further improves generated images.

In Table 6, we provide FID for generated images. For comparison, we include FID for ICNN-based [SCW₂B], and WGAN-QC (Liu et al., 2019). FID scores are adapted from (Korotin et al., 2021b, §4.5). Note that for $N = 1$, [SCW₂B] is reduced to the OT solver by (Makkuva et al., 2019) used as the loss for generative models, a setup tested in (Korotin et al., 2021b, Figure 3a). Serving as a generative model when $N = 1$, our algorithm 1 performs comparably to WGAN-QC and drastically outperforms ICNN-based [SCW₂B].

Method		FID↓
[SCW ₂ B]	$G_\xi(z)$	90.2
	$\hat{T}_{\mathbb{P}_\xi \rightarrow \mathbb{P}_1}(G_\xi(z))$	89.8
WGAN-QC	$G_\xi(z)$	14.4
Ours	$G_\xi(z)$	46.6
	$\hat{T}_{\mathbb{P}_\xi \rightarrow \mathbb{P}_1}(G_\xi(z))$	15.7
Ours (fixed G_ξ)	$G_\xi(z)$	N/A
	$\hat{T}_{\mathbb{P}_\xi \rightarrow \mathbb{P}_1}(G_\xi(z))$	16.1

Table 6: FID scores of generated faces.

Fixed generator. For $N = 1$, the fixed point approach §4.1 converges in only one step since operator \mathcal{H} immediately maps $G_\xi \# \mathbb{S}$ to \mathbb{P}_1 . As a result, in our algorithm 1, *exclusively* when $N = 1$, we can fix generator G_ξ and train only OT map T_{θ_1} from $G_\xi \# \mathbb{S}$ to data measure \mathbb{P}_1 and related potential v_{ω_1} . As a sanity check, we conduct such an experiment with randomly initialized generator network G_ξ . The results are given in Figure 8b, the FID is included in Table 6. Our algorithm performs well even *without generator training* at all.

C.3. Barycenters of MNIST Digits and FashionMNIST Classes

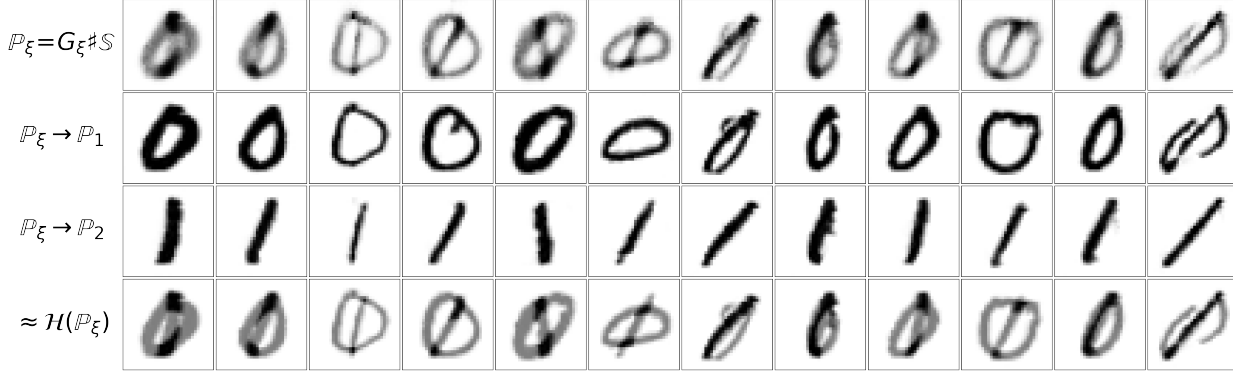
Similar to (Fan et al., 2020, Figure 6), we provide qualitative results of our algorithm applied to computing the barycenter of two MNIST classes of digits 0, 1. The barycenter w.r.t. weights $(\frac{1}{2}, \frac{1}{2})$ computed by our algorithm is shown in Figure 9. We also consider a more complex FashionMNIST (Xiao et al., 2017) dataset. Here we compute the barycenter of 10 classes w.r.t. weights $(\frac{1}{10}, \dots, \frac{1}{10})$. The results are given in Figures 10 and Figure 11.

Due to (6), each barycenter images are an average (in pixel space) of certain images from the input measure. In all

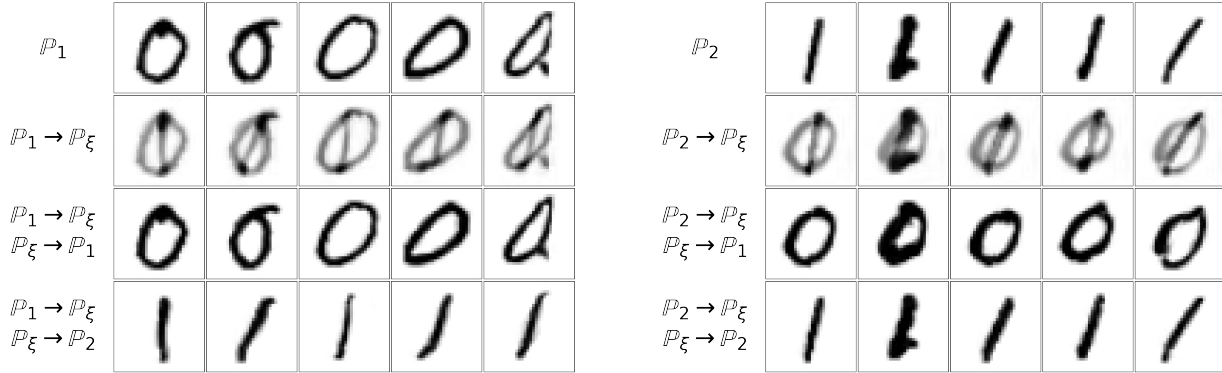
the Figures, the produced barycenter images satisfy this property. The maps to input measures are visually good. The approximate fixed point operator $\mathcal{H}(\mathbb{P}_\xi)$ is almost the identity as expected (the method converged).

C.4. Additional Results

In Figure 13, we visualize maps between Ave, Celeba! subsets through the learned barycenter. In Figure 12, we provide additional qualitative results for computing barycenters of Handbags, Shoes, Fruit360 datasets.



(a) The barycenter \mathbb{P}_ξ and maps to input measures \mathbb{P}_n .



(b) Samples from \mathbb{P}_1 mapped through \mathbb{P}_ξ to each \mathbb{P}_n .

(c) Samples from \mathbb{P}_2 mapped through \mathbb{P}_ξ to each \mathbb{P}_n .

Figure 9: The barycenter of MNIST digit classes 0/1 learned by Algorithm 1.

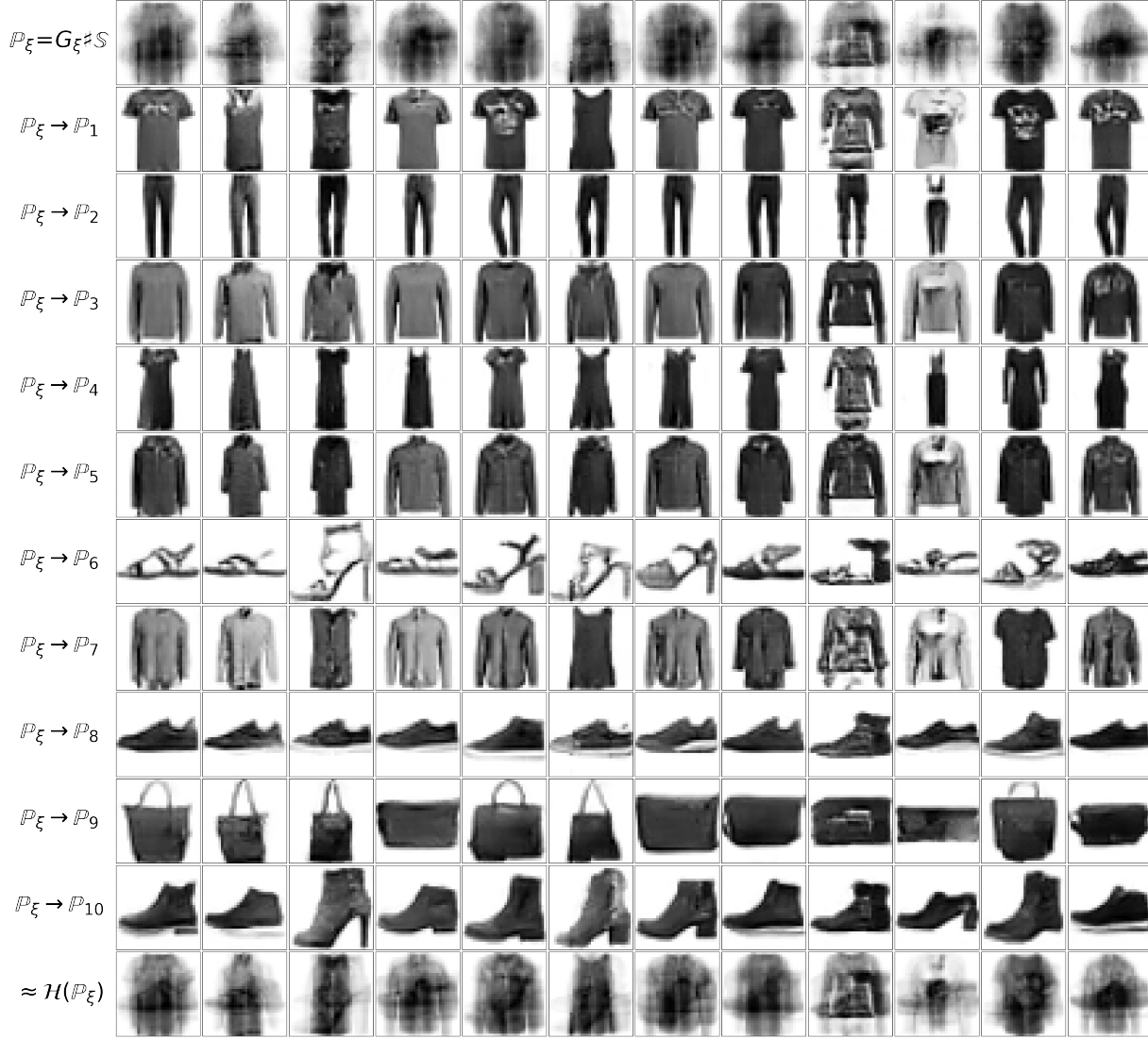


Figure 10: The barycenter and maps to input measures estimated by our method on 10 FashionMNIST classes (32×32). The 1st line shows generated samples from $\mathbb{P}_\xi = G_\xi \# \mathbb{S} \approx \mathbb{P}$. Each of 10 next lines shows estimated optimal maps $\hat{T}_{\mathbb{P}_\xi \rightarrow \mathbb{P}_n}$ to measures \mathbb{P}_n . The last line shows average $[\sum_{n=1}^N \alpha_n \hat{T}_{\mathbb{P}_\xi \rightarrow \mathbb{P}_n}] \# \mathbb{P}_\xi$.

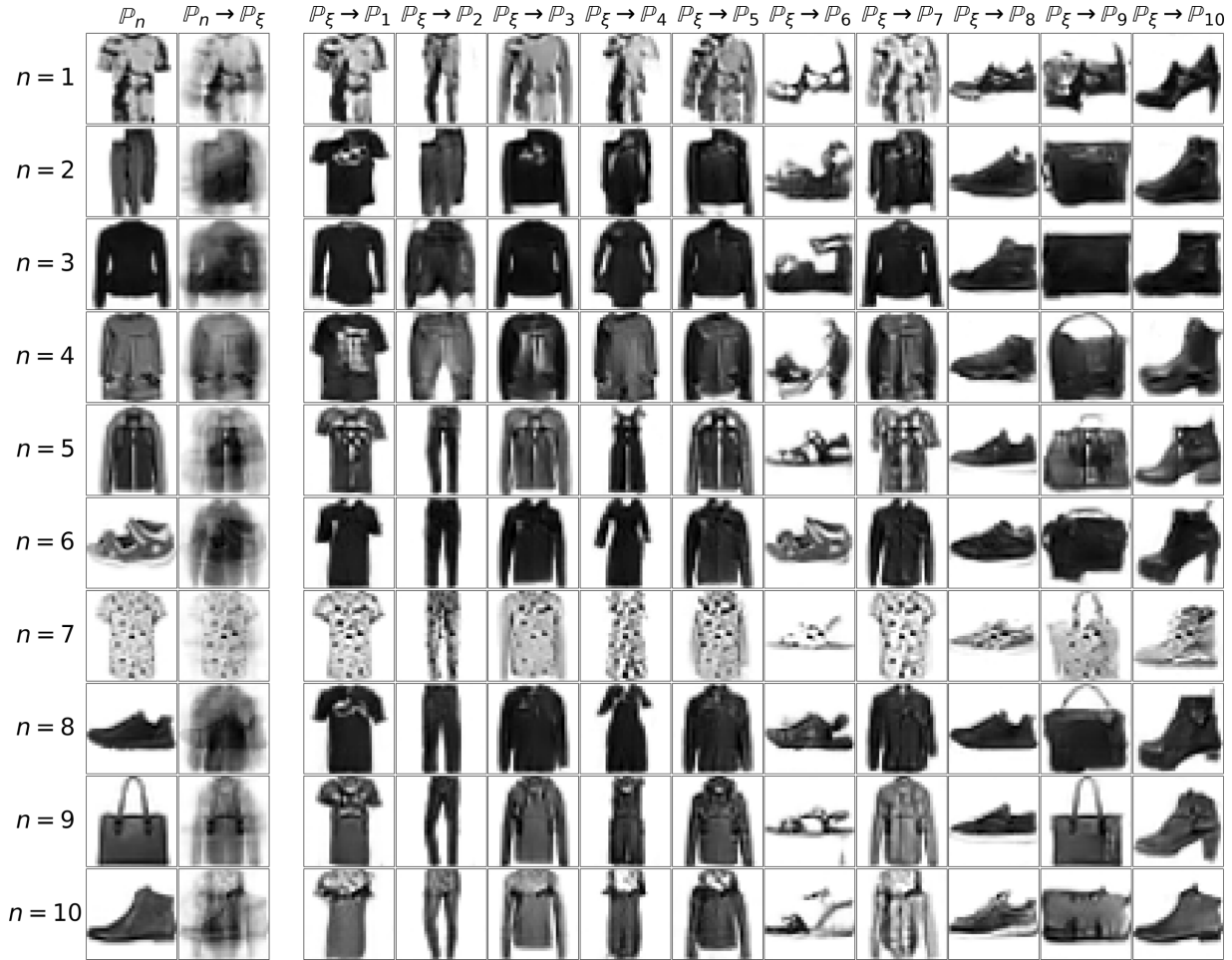
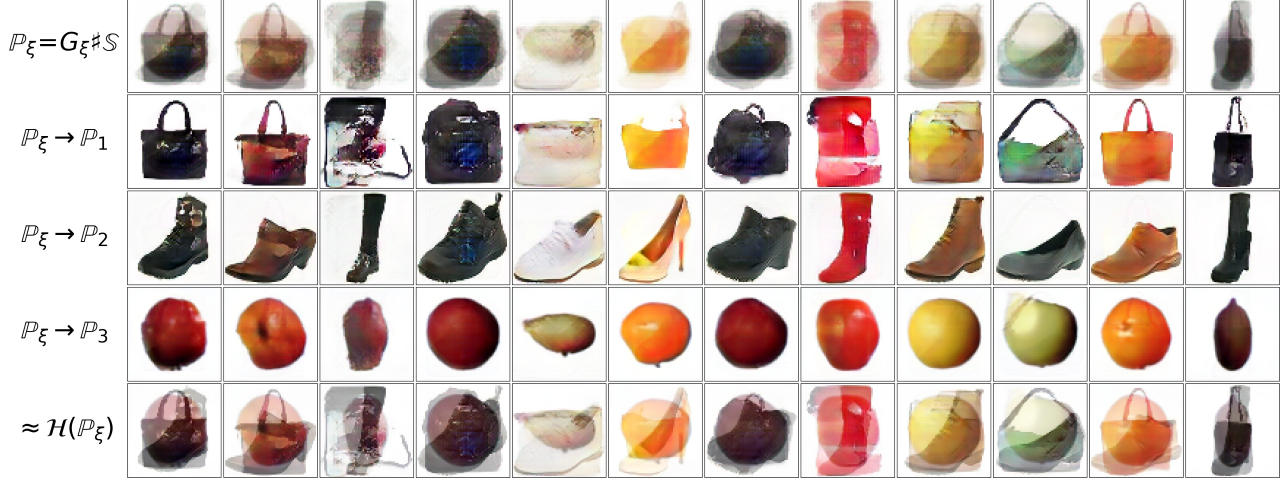
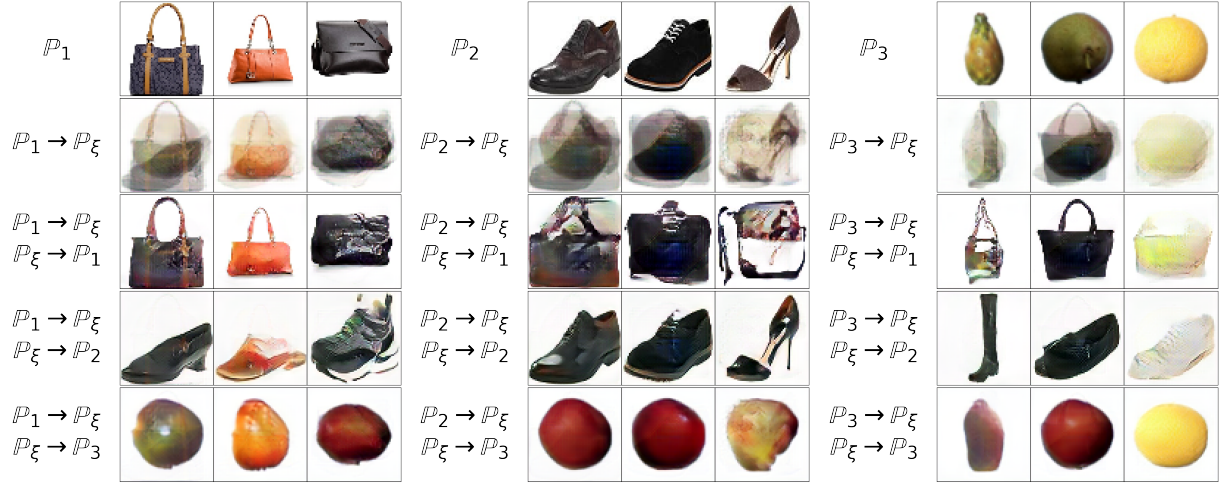


Figure 11: Maps between FashionMNIST classes through the learned barycenter. The 1st images in each n -th column shows a sample from \mathbb{P}_n . The 2nd columns maps these samples to the barycenter. Each next column shows how the maps from the barycenter to the input classes \mathbb{P}_n .


 (a) Generated samples $\mathbb{P}_\xi \approx \bar{\mathbb{P}}$, fitted maps to each \mathbb{P}_n and their average.

 (b) Samples $y \sim \mathbb{P}_1$ mapped through \mathbb{P}_ξ to each \mathbb{P}_n .

 (c) Samples $y \sim \mathbb{P}_2$ mapped through \mathbb{P}_ξ to each \mathbb{P}_n .

 (d) Samples $y \sim \mathbb{P}_3$ mapped through \mathbb{P}_ξ to each \mathbb{P}_n .

 Figure 12: The barycenter of Handbags, Shoes, Fruit (64×64) datasets fitted by our algorithm 1.

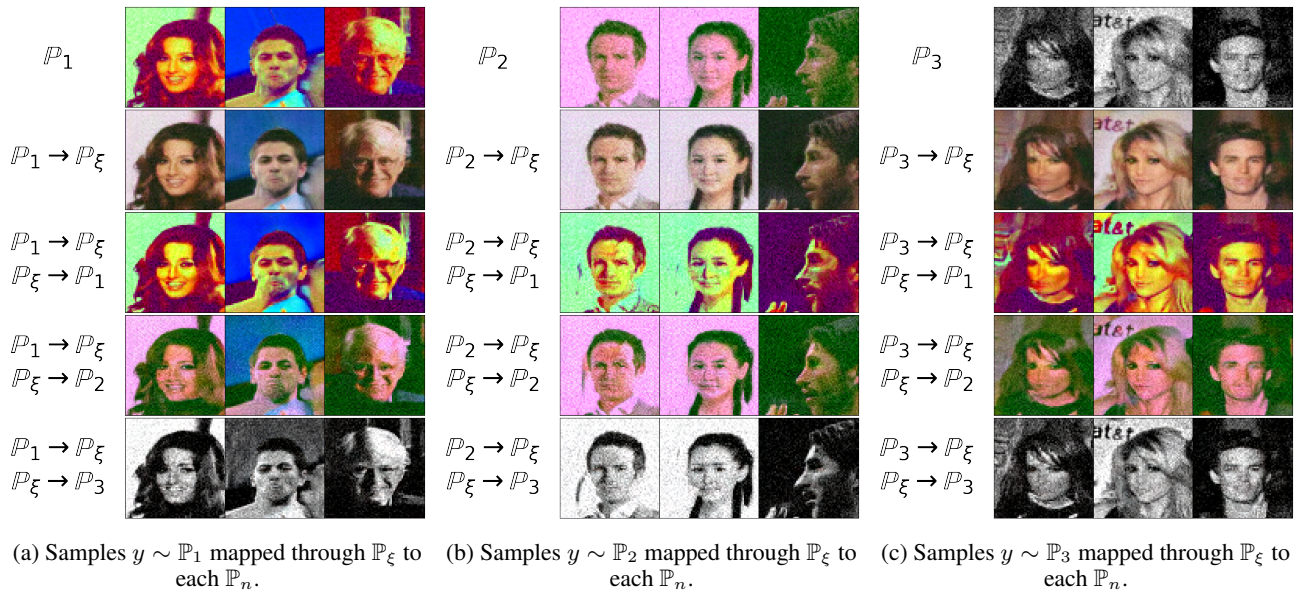


Figure 13: Maps between subsets of Ave, celeba! dataset through the barycenter learned by our algorithm 1.